



Slip Band Evolution Behavior near Circular Hole on Single Crystal Superalloy: Experiment and Simulation



Zixu Guo^{1,2}, Ziyuan Song¹, Xin Ding¹, Kaimin Guo³, Hongzhuo Liu¹, Han Yan¹, Dawei Huang^{1,5,*}, Xiaojun Yan^{1,4,5,*}

¹ School of Energy and Power Engineering, Beihang University, Beijing 100191, China

² Department of Mechanical Engineering, National University of Singapore, Singapore 117575, Singapore

³ Research Institute of Aero-Engine, Beihang University, Beijing 100191, China

⁴ National Key Laboratory of Science and Technology on Aero-Engine, Beijing 100191, China

⁵ Beijing Key Laboratory of Aero-Engine Structure and Strength, Beijing 100191, China

ARTICLE INFO

Keywords:

Single crystal superalloy
Film cooling hole
Slip band
Digital image correlation
Crystal plasticity

ABSTRACT

Circular holes on single crystal (SX) superalloys are widely utilized as film cooling structures on SX turbine blades, while their failure is a persistent issue. This study presents in-situ tests using digital image correlation (DIC) to reveal the slip band (SB) evolution behavior near the circular hole on SX superalloy, and proposes a mechanism-based model to capture the SB-associated evolutions of stress, strain, and damage fields. In the experiment part, high-temperature in-situ tensile tests are carried out under scanning electron microscope on plate-like SX specimens with circular hole, which can achieve the in-situ measurement and observation for the SB-induced strain concentration and microcrack nucleation. Experimental results reveal the effects of secondary orientation and temperature on stress-strain curve, SB evolution and SB direction. Besides, the microstructure observation shows that the γ phase shear is the primary cause of strain concentration inside SB. In the simulation part, a physics-based SB evolution model is proposed under the framework of crystal plasticity. For the regions inside and outside SB, different critical resolved shear stresses are utilized as the plasticity criteria, and different slip resistances are used as internal state variables in the flow rule to simulate the SB-induced strain concentration. A damage evolution rule is developed based on the plastic work density in slip systems to simulate the microcrack nucleation near the hole edge. Finally, the proposed model is validated through the experiments. The model can effectively simulate the SB initiation/evolution, SB direction, SB-induced strain concentration, and the microcrack nucleation near circular hole on SX superalloy.

1. Introduction

The turbine blade is a critical component of aeroengine, which operates in an environment with high temperature, high pressure, and high rotation speed. To ensure that the turbine blade can work reliably, two technical means have been applied. First, single crystal (SX) superalloys are used to prepare the turbine blade. The SX superalloys eliminate grain boundaries and use γ phases to impede the dislocation propagation, resulting in excellent mechanical properties in high temperatures (Cervellon et al., 2020; Chen et al., 2022;

* Corresponding authors at: No. 37 of Xueyuan Road, Beijing, China. Telephone number: +86-010-82316356
E-mail addresses: huangdawei@buaa.edu.cn (D. Huang), yanxiaojun@buaa.edu.cn (X. Yan).

Han et al., 2019). Secondly, the film cooling structure is designed on the blade body (Town et al., 2018; Zhang et al., 2020b). This structure is composed of hundreds of submillimeter-scale circular holes, which can form the cooling film on the blade body and isolate the high-temperature gas. However, since the circular holes damage the structural integrity of the blade, the stress and strain concentrate at the hole edge, leading to circular holes being the critical locations for failure (Ebrahimzade et al., 2021; Guo et al., 2019; Wang and Zhang, 2020). Under the action of mechanical load and temperature, the plasticity accumulation induced by the tensile load is the main reason for microcrack nucleation and failure at the hole edge (Fan et al., 2022; Guo et al., 2021b; Li et al., 2022a; Li et al., 2020; Yang et al., 2021; Zhang et al., 2020a). Therefore, it is necessary to investigate the mechanism and simulation method for the tensile behavior of circular hole on SX superalloy.

Temperature and secondary orientation are two significant factors that influence the tensile behavior of circular hole. There are primary and secondary orientations for circular holes on SX superalloy (Sabnis et al., 2012; Xiong Yukai, 2023; Zhou et al., 2019). The primary orientation is corresponding to the direction of tensile load, and the secondary orientation corresponds to the drilling direction of a circular hole. Previous investigations have paid more attention to the effects of primary orientation on tensile behavior and creep or fatigue life of circular hole (Wang et al., 2019; Wen et al., 2018; Zhang et al., 2020a). Since the mechanical properties of SX superalloy are anisotropic, the tensile behavior of circular hole should vary with the secondary orientation. Specifically, the stress/strain distributions and microcrack nucleation near circular hole are expected to vary with secondary orientation. However, it has not been widely concerned. Besides, the temperature is another important factor. As shown in the existing stress-strain curves (Huichen Yu, 2010), temperature significantly influences the yield and hardening behaviors of SX superalloy, which could impact the tensile behavior of circular hole on SX superalloy.

Existing experiments revealed that there are slip band (SB) initiation and evolution behaviors at the circular hole on SX superalloy under the tensile load. A lot of tensile tests for circular hole on SX superalloy can be found (Li et al., 2020; Li et al., 2019; Shang et al., 2019; Wen et al., 2018; Zhang et al., 2022; Zhou et al., 2019), which indicates that as the tensile load reaches a critical value, the SBs nucleate at the hole edge and tend to be wider upon the increase of load. Based on the microstructure observation of fracture, many slip traces can be found. These traces constitute the SB near the hole edge. For the region inside SB, the γ' phases have been heavily sheared and lose the ability to impede dislocations (Shang et al., 2019). Thus, theoretically speaking, the strain concentration should exist inside SB. Recently, the digital image correlation (DIC) technique was used to characterize the strain distribution near circular hole on SX superalloy at high temperature (Prastiti et al., 2020; Shang et al., 2019). In these works, a heat-resistant speckle pattern was prepared using Co_2O_3 powder, and the long focal-length microscope combined with a charge-coupled device camera was utilized to capture the speckle pattern. The strain concentration inside SB was observed. However, limited by the resolution of the microscope and camera, the minimum detectable crack length was as high as 0.2 mm (almost equal to the radius of the hole). So, the microcrack nucleation and evolution behaviors at the hole edge cannot be accurately captured. Besides, the high-temperature DIC method has not been applied to investigate the effects of temperature and secondary orientation on SB evolution and tensile behaviors for the circular hole on SX superalloy.

Some models arose to describe the SB evolution behavior. Based on the phase-field method or dislocation dynamics, SB evolution models were developed and applied to the simulation of stress/strain fields of material at the micro-level (Leslie T. Mushongera, 2020; Pagan and Beaudoin, 2019; Xu et al., 2021). These models can describe the strain concentration inside SB. However, limited by the computational efficiency, they cannot conduct the simulation on real structures such as a circular hole. In the framework of crystal plasticity finite element (CPFE), a SB evolution model was proposed (Chen et al., 2019; Zhou et al., 2006). To simulate the strain concentration inside SB, this model defined different types of flow rules for the regions inside and outside SB. However, these constitutive relations are not reliable enough, because it lacks physical evidence to use different flow rules at the regions inside and outside SB. Meanwhile, the simulated strain distribution and its evolution have not been validated by experiments. Besides, in this model, the SB initiation was simulated by embedding perturbations in the finite element (FE) model. It lacks the specific definition for the criterion of SB initiation, which conflicts with the existing experimental observations (Shang et al., 2019; Wen et al., 2018). Because existing experiments show that SB initiates as the external load reaches a threshold. Besides, the plasticity accumulation inside SB is the main reason for the failure of circular hole (Guo et al., 2021b; Li et al., 2020). But the existing models have not considered the modeling of damage evolution, so they cannot predict the microcrack nucleation of circular hole. Therefore, it is necessary to model the SB initiation and strain concentration based on the physical mechanism of plastic deformation for SB, and introduce the damage evolution equation into the flow rule.

In this paper, regarding the SB evolution behavior of the circular hole on SX superalloy, the investigations are conducted in the aspects of experiment and simulation. The main works are as follows. First, in-situ tensile tests are carried out at different temperatures and secondary orientations. The high-temperature DIC technique combined with scanning electron microscope (SEM) is employed to quantify the SB evolution and observe the microcrack nucleation/evolution. Secondly, a SB evolution model is proposed, which can capture the SB initiation/propagation, SB direction, SB-induced strain concentration, and microcrack nucleation of circular hole. Finally, the DIC measurement results are utilized to validate the proposed model.

2. In-situ tensile experiment

In this section, an in-situ tensile test system under SEM is developed. The high-temperature DIC technique is employed to measure the strain distribution near circular hole. Based on the above test method, the in-situ tensile tests are conducted on the specimen with and without circular hole at different secondary orientations and temperatures. The test results are discussed in the aspects of stress-strain curves, strain distributions, and microstructure evolution.

Table 1
chemical composition of the SX superalloy (in wt%).

W	Cr	Al	Co	Mo	Re	Ni
8.0	4.3	5.7	8.5	2.0	2.0	Balance

2.1. Material and specimens

The material used in this study is a second-generation Ni-based SX superalloy. The elemental mass percentages are listed in [Table 1](#). This SX superalloy contains 2% rhenium (by weight) to increase its strength at high temperatures. As shown in [Fig. 1](#), the initial microstructure is characterized by SEM and transmission electron microscope (TEM). The SEM image shows that the cubic γ' phases are evenly distributed in the γ phases. Based on the microstructure statistics method developed by our group ([Guo et al., 2022](#)), the volume fraction of γ' phases is 71%, and the average size of γ' phases is 366 nm. The average matrix channel width for γ phase is 50 nm. Besides, the TEM image shows that there are no obvious dislocations or stacking faults in both γ and γ' phases in the as-received state.

The plate-like specimens are used to conduct the in-situ tensile tests. The geometry of specimen is shown in [Fig. 2](#). The specimen without circular hole is employed to calibrate the parameters of SB evolution model. Meanwhile, the specimens with circular hole are employed to conduct the tests at different secondary orientations and temperatures. And they are also used to validate the CPFE simulation results. Moreover, the electro-stream machining technique is utilized to fabricate the circular hole on the center of specimen, which is same as the processing method of real film cooling structure on the turbine blade. This processing method can avoid forming the re-cast layer, oxidation layer, or corrosion layer at the hole channel ([Zhang et al., 2016](#)). The diameter of circular hole is 0.3 mm, which is a typical diameter for the real film cooling structure. The gauge length is 3 mm, which is used to measure the uniaxial strain of specimen center at macro-level.

The scheme of the experiment is listed in [Table 2](#). All the specimens have the same primary orientation (corresponding to the direction of tensile load) ([Fig. 2](#)). The unit vector \vec{O}_1 denotes the primary orientation, which is defined in the crystal coordinate system:

$$\vec{O}_1 = [\cos(\alpha_{[100]}), \cos(\alpha_{[010]}), \cos(\alpha_{[001]})] \quad (1)$$

where $\alpha_{[100]} / \alpha_{[010]} / \alpha_{[001]}$ are the angles between vector \vec{O}_1 and crystal orientation [100]/[010]/[001], respectively. The secondary orientation \vec{O}_2 (corresponding to the drilling direction of the hole) is expressed using the same method. The comparison between NH1-RT (RT denotes the room temperature) and H1-RT is used to reveal the effect of circular hole on the tensile behavior of SX superalloy. Besides, the H1-RT, H2-RT, and H3-RT are designed to investigate the effect of secondary orientation. It should be noted that the angles of secondary orientation between H1 and H2, H2 and H3 are 22.5°, respectively. Meanwhile, the H1-RT, H1-760, H1-850, H1-980 are employed to study the effect of temperature. The primary and secondary orientations for each specimen are listed in [Table 2](#), which are measured by EBSD (Swift, Oxford, UK).

2.2. Test method

The in-situ tensile test system under SEM is developed as follows. As shown in [Fig. 3 \(a\)](#), the micro tensile machine (SEMTester, MTI Instrument, USA) is mainly employed to apply tensile force on both ends of specimen, and the displacement rate is set to 0.2mm/min. During the test, the tension is paused several times to capture SEM images. The ceramic heater is used to heat the specimen to the pre-determined temperature. The cyclic cooling water is applied to the heater in case of overheating. Meanwhile, the SEM (EVO18, Carl Zeiss, Germany) is utilized to observe the region of interest. As shown in [Fig. 3 \(b\)](#), before the test, two parallel lines (3 mm distance) are marked on the specimen using the laser. It is used as gauge length to measure the uniaxial average strain $\bar{\epsilon}$. Besides, during the tensile test, the working distance of SEM is kept as 10mm by adjusting the height of stage, which is to avoid the out-plane deformation of specimen and ensure the accuracy of DIC test.

To conduct the DIC measurement, the surface of specimen is specially treated before the test. The region near the circular hole is divided into region A and region B. The region A shown in [Fig. 3 \(c\)](#) is used to conduct the DIC measurement. A kind of heat-resistant speckle pattern is prepared on region A. The processing method is as follows. First, the surface of specimen is finely polished. Then, ZrO_2 powder (particle size=25 μm) is mixed with alcohol to prepare the solution. Ultrasonic shock is utilized to disperse the ZrO_2 particles in the solution. After that, the 0.15 μL solution is dropped to region A using a pipette gun (Hipipette, DLAB, China). After the evaporation, the speckle pattern shown in [Fig. 3 \(c\)](#) can be obtained. This speckle can withstand high temperatures of up to 1000°C and is unlikely to disintegrate for extended periods (around 100 hours). To evaluate the quality of the speckle pattern, the Glare software is employed to calculate the average diameter d_s for the prepared speckle ([Su and Zhang, 2022](#)). The Glare indicates that d_s equals 3.21 pixels. Empirically, the reasonable value of d_s is between 3 to 5 pixels ([Forssström et al., 2020; Zhu et al., 2022](#)). So, the prepared speckle pattern has acceptable quality. To finally obtain the strain distribution, an open-source program called Ncorr is utilized to post-process the speckle patterns before and after deformation ([Blaber et al., 2015](#)). Meanwhile, as shown in [Fig. 3 \(d\)](#), the metallographic corrosion is performed at region B using the solution of 25 ml HCl + 5 ml H_2SO_4 + 5 g $CuSO_4$ + 20 ml H_2O . The corrosion time is 8 s. After that, the γ/γ' phases near circular hole can be seen clearly under SEM, which are used to observe the microcrack nucleation behaviors during the in-situ tension, and validate the prediction of microcrack nucleation given by the damage evolution model. Besides, the γ/γ' phases can also be used as speckle pattern to measure the strain distribution in micro-scale.

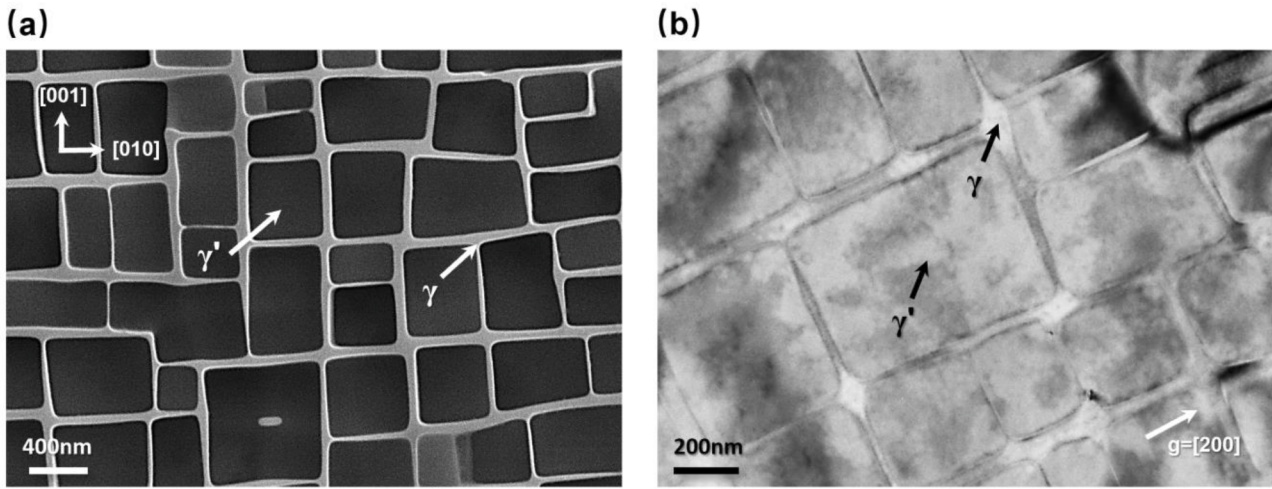


Fig. 1. microstructure of the as-received SX superalloy: (a) SEM image; (b) TEM image.

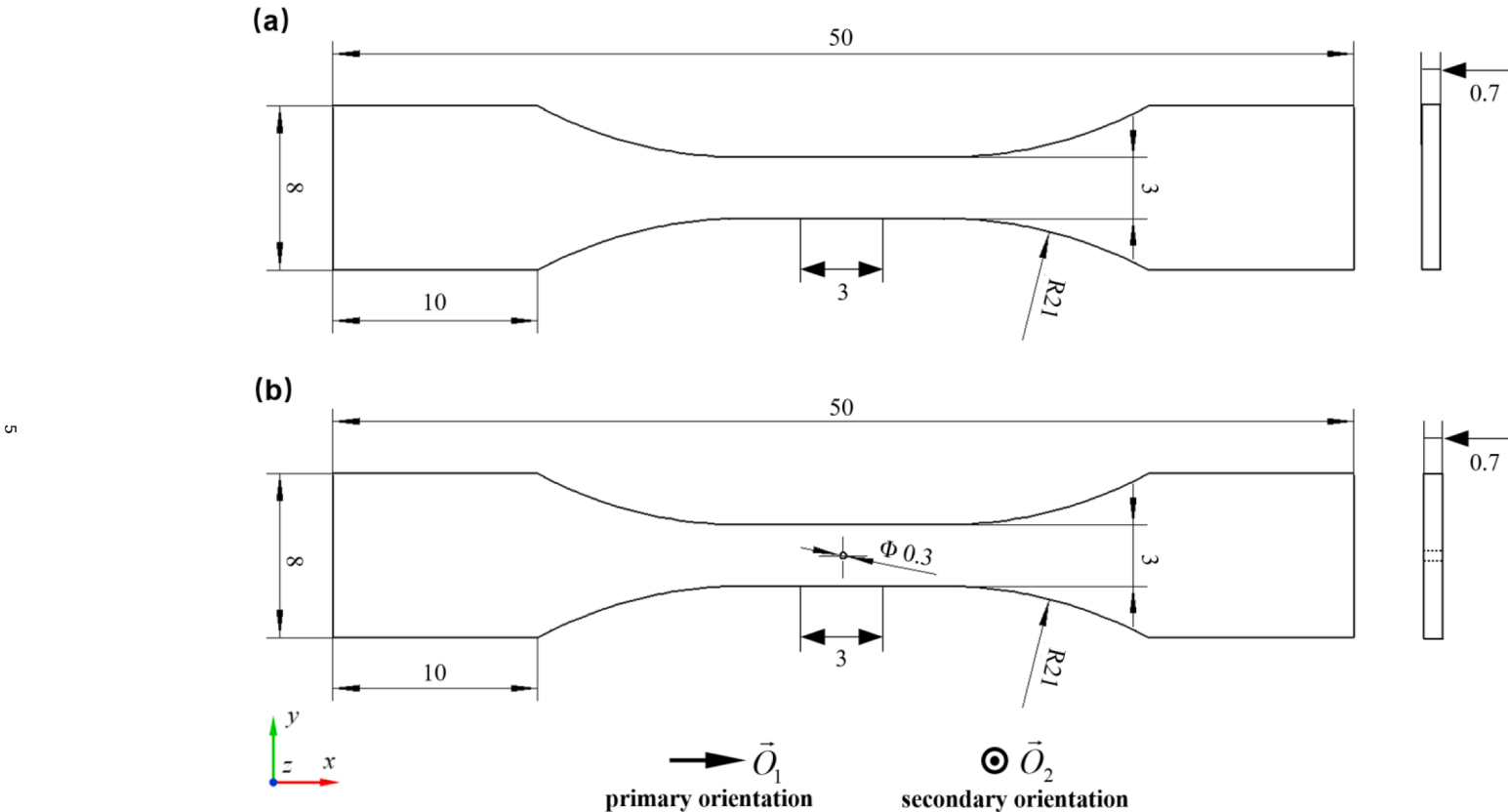


Fig. 2. plate-like specimens (unit: mm): (a) specimen without a circular hole; (b) specimen with a circular hole.

Table 2
scheme of in-situ tensile tests.

Test NO.	specimen	primary orientation \vec{O}_1 [-0.9985, 0.0173, 0.0521]	secondary orientation \vec{O}_2 [0.0520, 0.0055, 0.9986]	temperature/°C room temperature
NH1-RT	without hole			
H1-RT	with single circular hole			
H2-RT			[0.0457, -0.2641, 0.9634]	
H3-RT			[0.0244, -0.7109, 0.7029]	
H1-760			[0.0520, 0.0055, 0.9986]	760
H1-850				850
H1-980				980

2.3. Test Results

Based on the above test method, the in-situ tensile tests are conducted at different secondary orientations and temperatures. First, the stress-strain curves are analyzed to unveil the mechanical properties of specimens under different test conditions. Then, based on the strain distribution measured by DIC, the SB evolution behavior is discussed. Finally, the microstructure observation is conducted to investigate the mechanisms of strain concentration and microcrack nucleation.

2.3.1. Stress-strain curves

Regarding different test conditions shown in Table 2, the stress-strain curves are analyzed as follows. First, it should be noted that the stress mentioned in Fig. 4 is the nominal stress $\bar{\sigma}$ that is calculated using the sectional area without considering the area reduction caused by circular hole. Besides, the end of each curve is corresponding to the stress and strain that microcrack can be observed by SEM. As shown in Fig. 4 (a), by comparing NH1-RT and H1-RT, it can be found that after the fabrication of circular hole, the yield stress, ultimate tensile strength, and $\bar{\epsilon}$ at microcrack nucleation decrease obviously. Meanwhile, by comparing H1-RT, H2-RT, and H3-RT, the secondary orientation has a slight effect on stress-strain curves. This difference is caused by the quantity distribution of the activated slip system near hole edge (Xiong Yukai, 2023). Besides, as shown in Fig. 4 (b), it can be seen that temperature has a significant effect on stress-strain curves, which is caused by the variation of mechanical properties for SX superalloy at different temperatures.

2.3.2. Strain distributions

The comparison of strain distribution between the specimens with and without circular hole is discussed as follows. The evolution of strain distribution for NH1-RT is shown in Fig. 5. As the stress $\bar{\sigma}$ and strain $\bar{\epsilon}$ are 835 MPa and 0.006, the strain distribution is relatively homogeneous, and the SB has not initiated. When $\bar{\sigma}$ and $\bar{\epsilon}$ increase to 1075 MPa and 0.095, the strain concentrates on some band-like regions that are induced by the initiation of SBs. These activated SBs all belong to (1-11) slip plane, because this slip system has the highest Schmid factor. As $\bar{\sigma}$ and $\bar{\epsilon}$ reach 1094 MPa and 0.117, the SBs tend to be wider and have a higher fraction. Meanwhile, the strain level inside SB becomes higher. For comparison, the first row of Fig. 6 shows the evolution of strain distribution for H1-RT. After the fabrication of circular hole, the $\bar{\sigma}$ corresponding to SB initiation decreases to around 650 MPa. The stress and strain concentrations at the hole edge are the main reasons for the earlier SB initiation. Besides, there are two activated SBs near the hole. These two SBs have different directions, which are corresponding to (1-11) and (-1-11) slip planes of SX. When the $\bar{\sigma}$ increases to 770 MPa, these two SBs become wider and have higher strain level.

The evolution of strain distribution at different secondary orientations is shown in Fig. 6. As $\bar{\sigma} = 400$ MPa, the strain concentrates at the hole edge, but the SBs have not come into being for H1, H2, H3 specimens. When the stress reaches about 650 MPa, the SBs initiate at the hole edge, and the SB direction varies with secondary orientation. As the stress increases to 770 MPa, the SBs become wider, and the strain inside SB becomes higher. For the H1 specimen, two SBs at the hole edge are approximately symmetrical along the y axis, with similar width and strain level. For the H2 and H3 specimens, two SBs are unsymmetrical. There are primary SB and secondary SB at the hole edge. Compared to the secondary SB, the primary SB initiates earlier and has higher width and strain level.

The evolution of strain distributions at different temperatures is shown in Fig. 7, which takes H1-850 and H1-980 as examples. After applying high temperature, the slip systems of activated SBs at the hole edge are the same as that at room temperature. So, the SBs are still symmetrical, and the SB directions remain unchanged. Nevertheless, the critical nominal stress of SB initiation varies with temperature obviously, which follows the order of H1-850 > H1-RT > H1-980. For the H1-850 specimen, the SB initiates as the $\bar{\sigma}$ reaches around 680 MPa, while this critical nominal stress decreases to about 530 MPa for H1-980.

2.3.3. Microstructure observation

Taking H2-RT as an example, after SB initiation, the microstructures inside and outside SB are characterized by SEM and TEM (Fig. 8). For the region outside SB, as shown in Fig. 8 (b), plasticity does not affect the morphology of γ/γ' phases. The γ/γ' phases are the same as the initial microstructure shown in Fig. 1 (a). Meanwhile, as shown in Fig. 8 (c), the TEM observation indicates that some dislocations exist in the matrix channel. Most of these dislocations pile up at the interfaces of γ/γ' phases and lead to dislocation hardening. This means that the stacked dislocation will generate resistance to subsequent dislocations, resulting in an increase of yield limit. Some dislocations within matrix channel bypass γ' phases based on the Orowan mechanism (Barnett et al., 2019; Fomin et al., 2021). The γ' phases can still impede dislocation motion. In this situation, the plasticity mechanism is named as mechanism (i).

For the region inside SB, as shown in Fig. 8 (d), some slip traces can be observed. These traces have the same direction as SB. It can

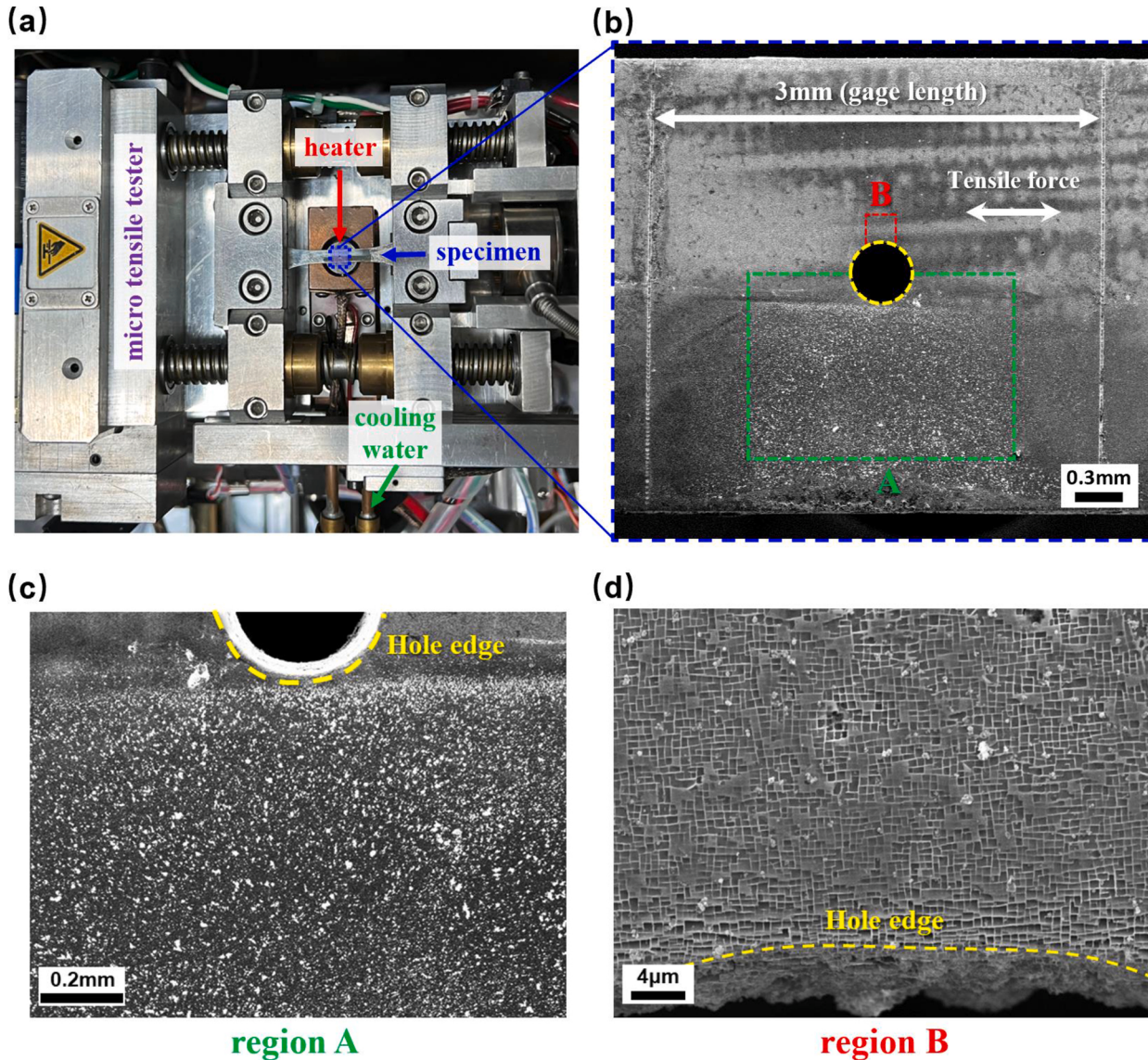


Fig. 3. tensile test system and the specimen after special treatment: (a) in-situ tensile test system; (b) region of interest for the specimen after sample preparation; (c) region A for DIC measurement; (d) region B for the observation of microcrack nucleation.

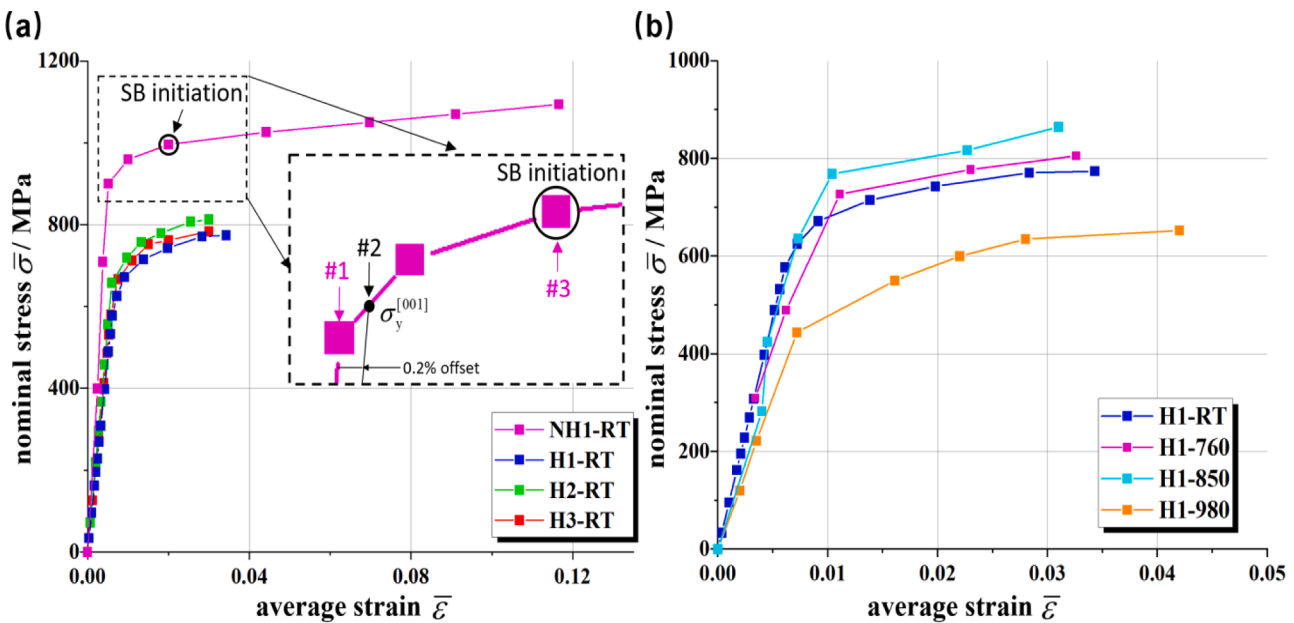


Fig. 4. measured stress-strain curves: (a) comparison at different secondary orientations; (b) comparison at different temperatures.

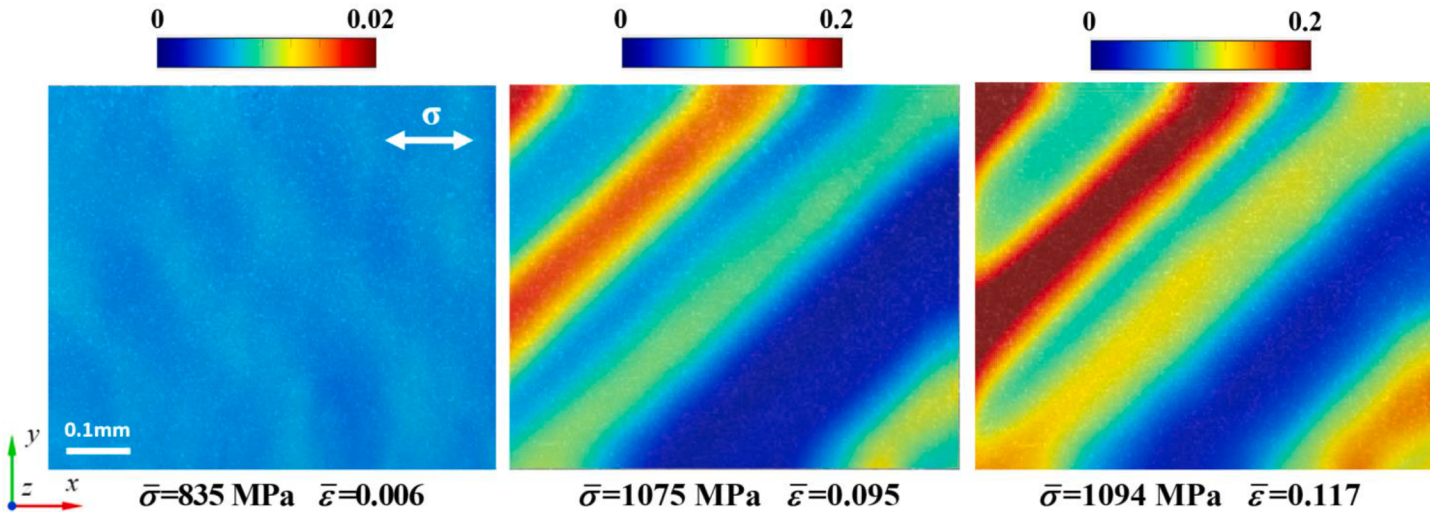


Fig. 5. the evolution of total strain distribution (ε_{xx}) for the NH1 specimen.

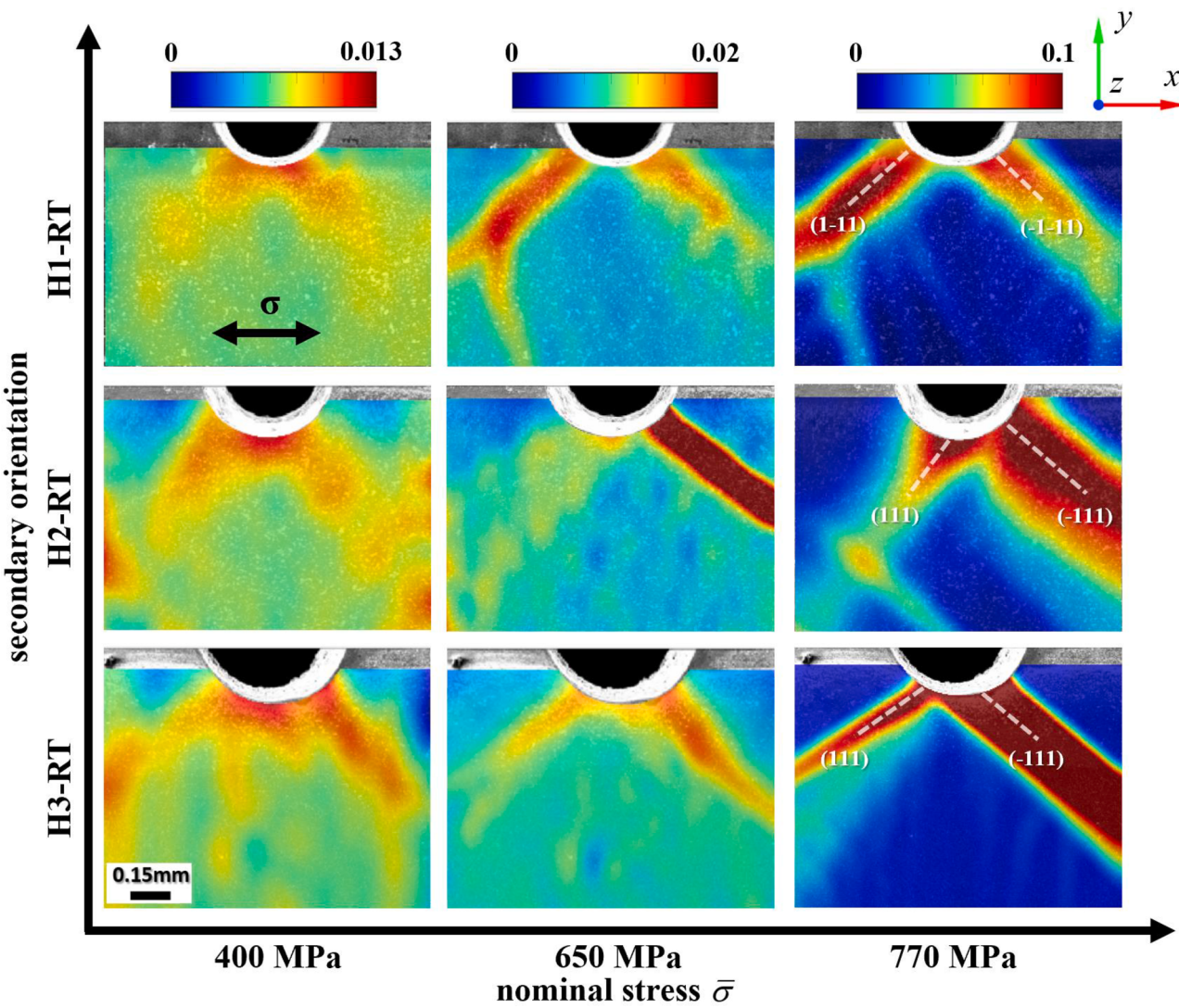


Fig. 6. the evolution of total strain distribution (ε_{xx}) at different secondary orientations.

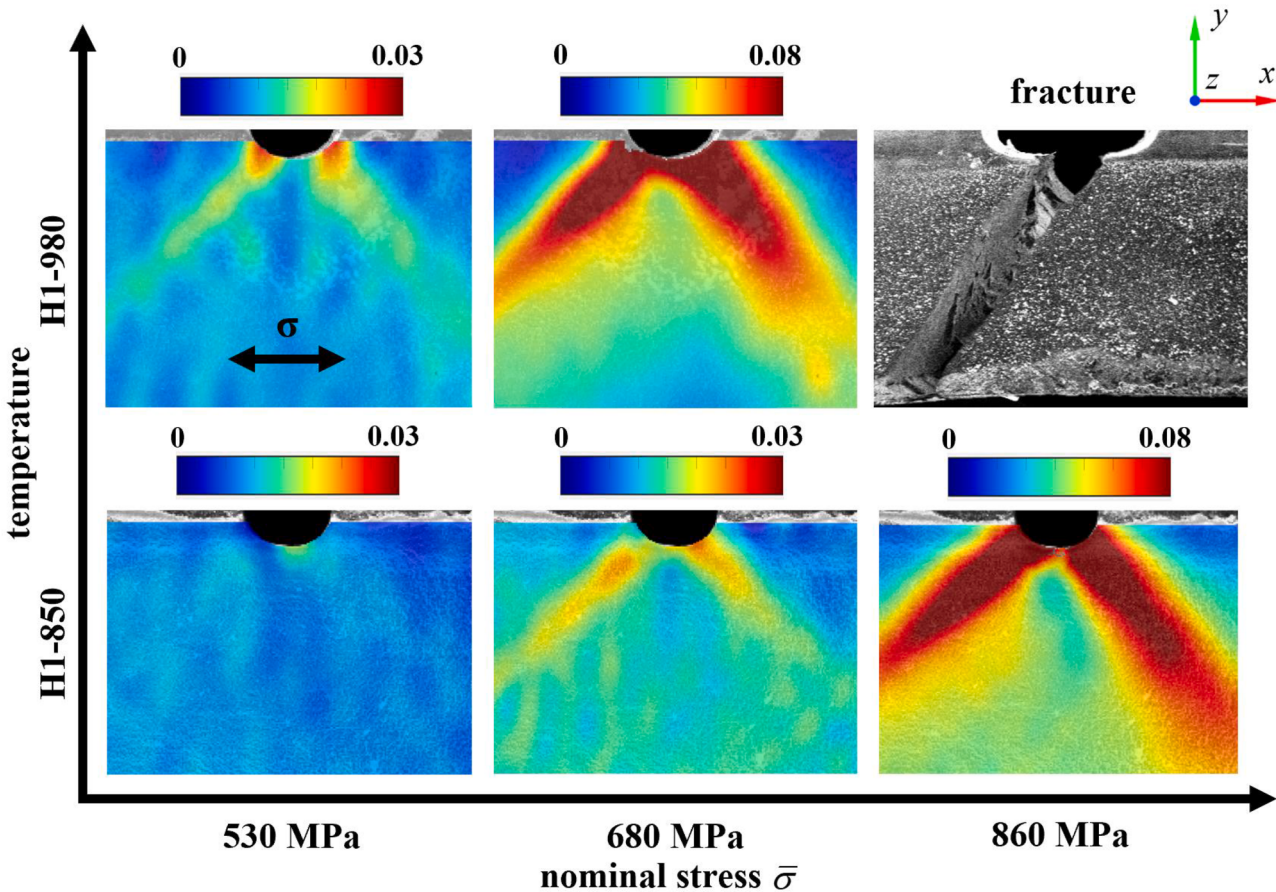


Fig. 7. the evolution of total strain distribution (ϵ_{xx}) at different temperatures.

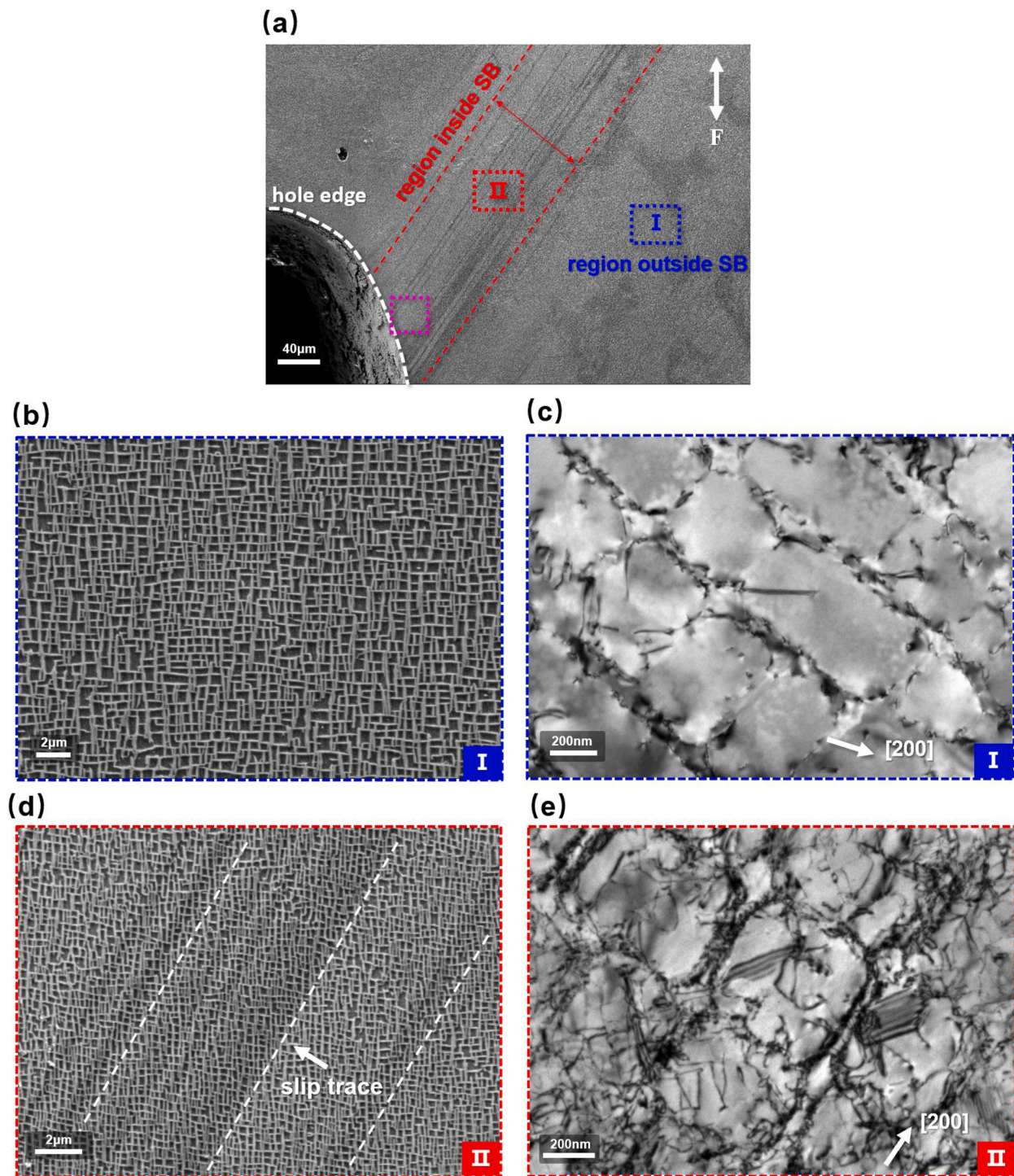


Fig. 8. microstructure near circular hole after SB initiation: (a) macro morphology after SB initiation; (b)-(c) SEM and TEM images for the region outside SB; (d)-(e) SEM and TEM images for the region inside SB.

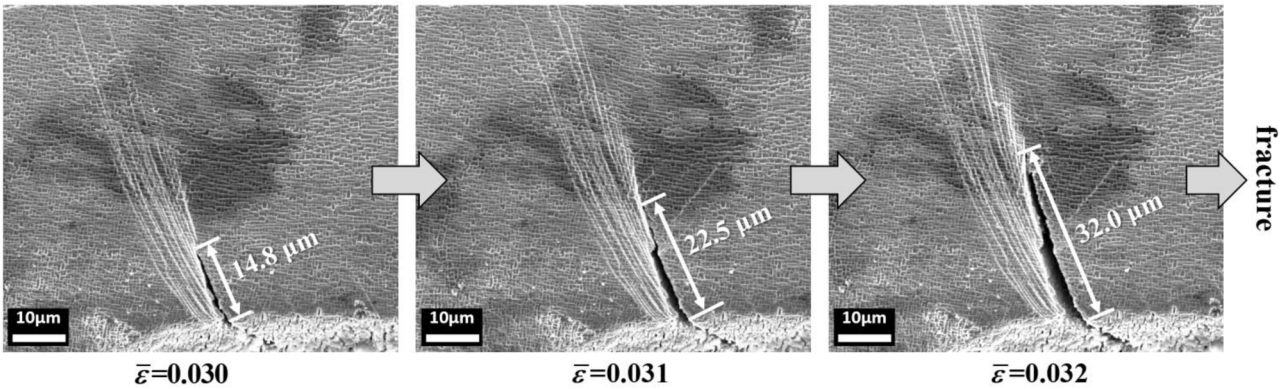


Fig. 9. microcrack nucleation and propagation behaviors inside SB.

be proved that the strain concentrates at slip traces, by using γ/γ' phases as speckle pattern to conduct the DIC measurement. Meanwhile, as shown in Fig. 8 (e), the TEM observation shows that there are lots of dislocations inside γ' phases, and some of the dislocations resolve into stacking faults. So, the γ' phases are substantially sheared by the dislocations and lose the ability to impede the dislocation multiplication, which means that the γ' phase-associated dislocation hardening and bypassing no longer have any effect. The reduction of slip resistance leads to the strain concentration inside SB. Besides, judging by the directions of horizontal and vertical matrix channels in Fig. 8 (d), no obvious crystal orientation change exists inside SB, which also can be found in previous works (Larrouy et al., 2015; Wang et al., 2022). In this situation, the plastic deformation mechanism is named as mechanism (ii).

Besides, it should be noted that the qualitative mechanism of plasticity at room temperature is similar to the mechanism at high temperatures under tensile test (Shang et al., 2019). Because, the test duration is too short to lead the obvious γ/γ' microstructure evolution (dissolution and rafting of γ' phase) and enough diffusion-controlled plasticity at high temperatures. Moreover, as shown in Fig. 14 (b) and Fig. 16 (d), the model developed based on the above deformation mechanism at room temperature can effectively capture the stress-strain curves and SB evolutions at high temperatures.

As the load is high enough, microcrack nucleation and evolution can be observed at the tip of SB (Fig. 9). The region of Fig. 9 corresponds to the purple box in Fig. 8 (a). As the plasticity inside SB accumulates to a critical value, the continuity of material will be destroyed, and then the microcrack comes into being. The microcrack growth is rapid, and eventually leads to fracture. Meanwhile, the crack propagation stage is short, accounting for only 6.3% of total deformation (the proportion of $\bar{\epsilon}$). Since the subsequent modeling of damage evolution does not consider the crack propagation stage, the microcrack nucleation that can be observed is defined as the criterion of failure in experiment, and the $\bar{\epsilon}$ at microcrack nucleation is used to validate the damage evolution model.

3. CPFE simulation

In this part, under the framework of CP theory, a mechanism-based SB evolution model is proposed, which can capture SB initiation/evolution, SB direction, SB-induced strain concentration, and microcrack nucleation of circular hole. After that, the FE implementation method for the proposed model is developed. Finally, parameters in proposed model are calibrated, and the FE model is established to conduct the simulation.

3.1. CP theory

The simulation is conducted under the framework of CP. Only a brief introduction to CP model is given here, and the details can be found in the references (Dunne et al., 2007; Xu et al., 2022).

First, the total deformation gradient $[F]$ is decomposed into elastic $[F_e]$ and plastic $[F_p]$ deformation gradients:

$$[F] = [F_e][F_p] \quad (2)$$

Then, the increment of plastic strain tensor $[de_p]_c$ in crystal coordinate can be expressed by $[F_p]$ (Xu et al., 2022):

$$[de_p]_c = [dF_p][F_p]^{-1} = \sum_{s=1}^{12} ([n^s] \otimes [m^s]) d\gamma^s \quad (3)$$

where $[m^s]$ is the unit vector normal to the slip plane, $[n^s]$ is the unit vector along the slip system, $d\gamma^s$ is the increment of plastic resolved shear strain. The SX superalloy has face-centered cubic (FCC) lattice. Octahedral slip system has the highest priority to be activated (Gupta and Bronkhorst, 2021; Prastiti et al., 2020). The variable s denotes the index of slip system and varies from 1 to 12. The $d\gamma^s$ is calculated by the flow rule, which will be developed in Section 3.2.

Besides, the resolved shear stress (RSS) is expressed as follows:

$$\tau^s = [P^s] : [\sigma]_c \quad (4)$$

where τ^s is the RSS, $[\sigma]_c$ is the stress tensor in crystal coordinate system, and $[P^s]$ is the Schmid factor that can be calculated as follows:

$$[P^s] = \frac{1}{2} ([m^s][n^s]^T + [n^s][m^s]^T) \quad (5)$$

Besides, it should be noted that the stress/strain tensors in crystal coordinate system (Eq. (4) and Eq (3)) are connected with stress/strain in the global coordinate system via the transformation principle of tensor.

3.2. SB evolution model

In this part, to simulate the SB initiation, different physics-based critical resolved shear stresses (CRSSs) are utilized as the plasticity criteria for the regions inside and outside SB. Besides, to capture the strain concentration inside SB, different physics-based slip resistances are employed as internal state variables in the same flow rule for the regions inside and outside SB. Then, to simulate the microcrack nucleation near circular hole, the damage evolution equation is developed and coupled with the flow rule.

For the regions inside and outside SB, a unified rate-independent flow rule is utilized to calculate the increment of resolved shear strain in each slip system:

$$d\gamma^s = \left(\frac{|\tau^s| - r^s}{\tau_0} \right)^n d\tau^s \left(|\tau^s| > r^s \right) \quad (6)$$

where r^s is the resistance of dislocation motion, n and τ_0 are the exponent and coefficient in flow rule. In this flow rule, the loading condition is defined as $\tau^s d\tau^s > 0$, and the $|\tau^s| - r^s$ is considered as the effective RSS that actually drives the dislocation motion and plasticity accumulation, and the power law is used to describe the relationship between effective RSS and growth rate of plastic resolved shear strain. Besides, it should be noted that under the framework of rate-independent CP model, the plastic resolved shear strain rate is generally described by $d\gamma^s/d\tau^s$, rather than $d\gamma^s/dt$ (t denotes the time) (Fathallah et al., 2019; Forest and Rubin, 2016; Kothari, 1995). Moreover, viscoplasticity is not considered in this flow rule. Because, for the tensile behavior investigated in this work, the physical time is too limited (lower than 1 hour) to generate enough viscoplasticity that can significantly influence the stress and strain fields.

Besides, to simulate the microcrack nucleation, the damage variable D^s is defined in the slip systems. The rule of damage evolution is expressed using the plastic work density W_p^s in slip system:

$$dD^s = \frac{W_p^s}{W_{cr}} = \frac{\tau^s d\gamma^s}{W_{cr}} \quad (7)$$

where W_{cr} is the critical plastic work density. The damage variable represents the proportion of atomic vacancies resulting from dislocations either piling up at the interfaces of γ/γ' phases or bypassing γ phases in slip systems. The microcrack nucleates as the fraction of vacancy accumulates to a threshold. This is the foundation of most damage-coupled CP models (Cormier and Cailletaud, 2010; Ma et al., 2008; Yin et al., 2022; Zhang et al., 2019). The plastic work from external load is the primary driving force for the accumulation of the dislocation-associated vacancy. Because, the plastic work can transform into thermal dissipation energy and plastic stored energy, and the stored energy can be expressed by the dislocation density ρ^s in slip system (Sendrowicz et al., 2022):

$$\eta W_p^s \propto \beta G b^2 \rho^s \quad (8)$$

where η is the efficiency that plastic work converts to the stored energy, β is a constant, b is the norm of burgers vector, G is the shear module corresponding to the direction of slip system. From Eq. (8), the W_p^s is proportional to dislocation density ρ^s that measures the fraction of vacancy. Therefore, it is reasonable to use plastic work as the driving force of damage evolution. Besides, since the SX superalloy used in this study has very small amount of pores, and the pores cannot be observed at the fracture surface, the effect of pore growth on damage evolution is not considered.

Meanwhile, the W_{cr} in Eq. (7) denotes the critical value of plastic work density that can be accommodated in slip system, which is associated with critical dislocation density of microcrack nucleation. As the plastic work density in slip system reaches W_{cr} , the proportion of atomic vacancy accumulates to 1. As the plastic work density is lower than W_{cr} , the Eq. (7) assumes that the proportion of atomic vacancy changes linearly with plastic work density, which can be validated in Section 4.1. Besides, the determination method for W_{cr} is illustrated in Section 3.4. The D^s varies from 0 to 1. Microcrack nucleates at the region inside SB where the maximum D^s among all slip systems reaches 1.

The coupling between the damage variable and flow rule is illustrated as follows. The vacancy-associated damage variable can lead to the reduction of the effective bearing area in slip system. So, the RSS needs to be replaced as equivalent RSS $\tilde{\tau}^s$, which is based on the principle of strain equivalence proposed by Lemaître (Lemaître, 1985):

$$\tilde{\tau}^s = \frac{\tau^s}{(1 - D^s)} \quad (9)$$

This transformation has been widely used in some damage-coupled CP models (Cormier and Cailletaud, 2010; Yin et al., 2022; Zhang et al., 2019). Thus, the flow rule in Eq.(6) is re-written as:

$$d\gamma^s = \left(\frac{|\tilde{\tau}^s| - r^s}{\tau_0} \right)^n d\tilde{\tau}^s \quad (10)$$

For the region outside SB where deformation mechanism (i) (discussed in Section 2.3.3) happens, the observed mechanisms including dislocation hardening and dislocation bypassing are involved in the slip resistance:

$$r_1^s = r_{\text{dislocation}}^s + r_{\text{bypassing}}^s + r_{\text{lattice}}^s \quad (11)$$

where r_1^s is the slip resistance for the region outside SB. The $r_{\text{dislocation}}^s$ denotes the contribution of dislocation hardening, which is caused by the resistance from existing dislocations stacked at γ/γ' interfaces to subsequent dislocations. The $r_{\text{dislocation}}^s$ is also used to capture the change of yield surface after plastic deformation. Besides, the $r_{\text{bypassing}}^s$ is employed to consider the mechanism of dislocation bypassing γ phase. The r_{lattice}^s is the increment of slip resistance caused by lattice resistance, which is a constant for SX superalloy. Moreover, the RSS needs to overcome the CRSS to generate plasticity. So, the criterion for the occurrence of mechanism (i) is written as:

$$|\tau^s| \geq r_{\text{dislocation}}^s + r_{\text{bypassing}}^s + r_{\text{lattice}}^s \quad (12)$$

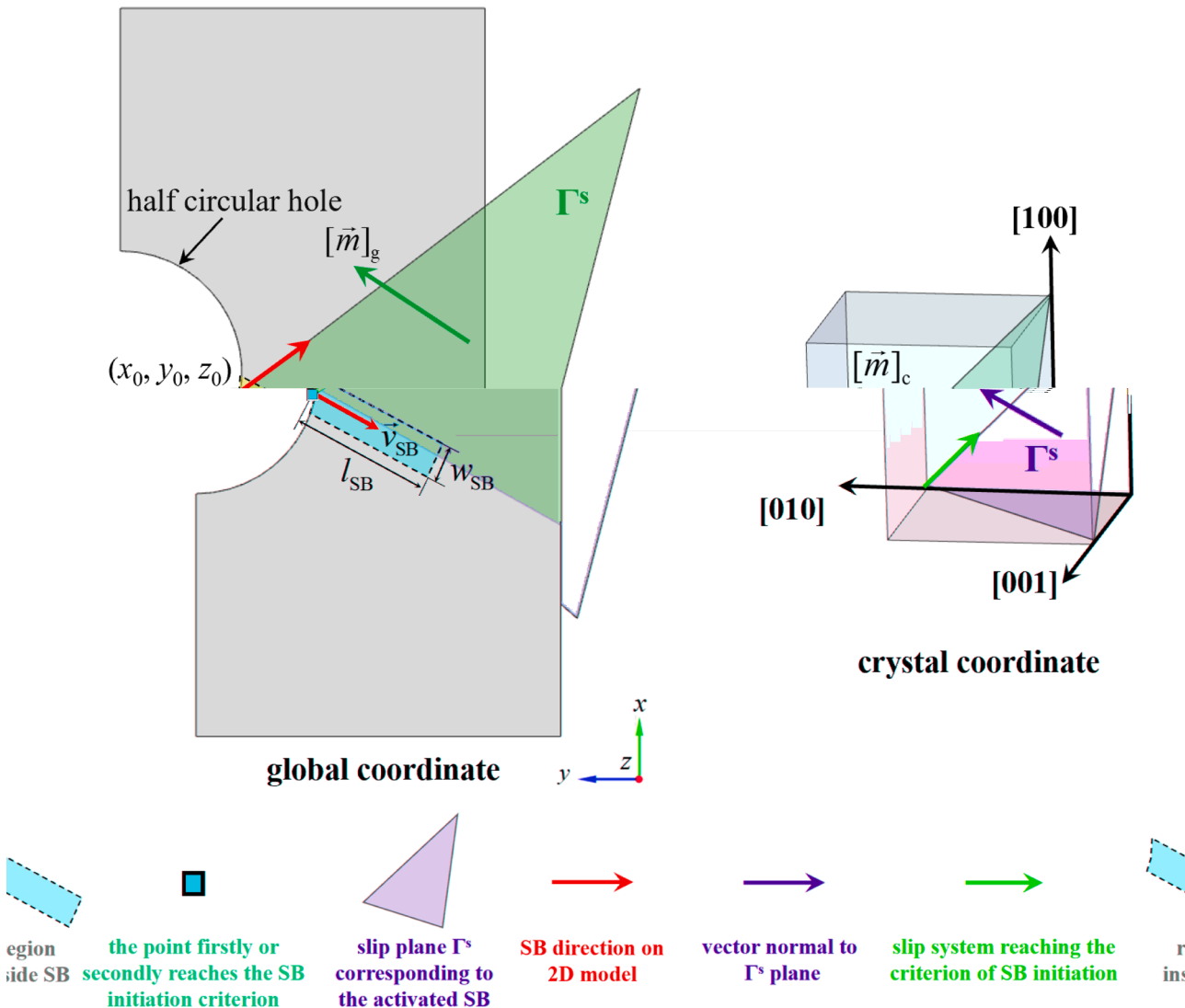


Fig. 10. schematic diagram of SB evolution modeling.

Furthermore, as discussed in [Section 2.3.3](#), the SB initiates as the RSS reaches the critical value that γ' phases can be sheared by dislocations:

$$|\tau^s| \geq (r_{\text{shear}}^s + H^s) \quad (13)$$

where r_{shear}^s is the CRSS of γ' phase shear that is determined based on the energy of anti-phase boundary (APB) within γ' phases ([Reed, 2008](#)). The H^s initialized with a value of 0 is used to record the highest RSS in the slip system following the occurrence of mechanism (ii), allowing for the isotropic hardening and the change of yield surface. Meanwhile, as discussed in [2.3.3 Microstructure observation](#), there is no obvious crystal orientation difference inside and outside SB. So, during the simulation, the crystal orientation remains unchanged for the region inside SB. After SB initiation, only lattice resistance needs to be considered:

$$r_2^s = r_{\text{lattice}}^s \quad (14)$$

For the flow rule in [Eq. \(10\)](#), the r^s is replaced as r_1^s for the region outside SB, and replaced as r_2^s for the region inside SB, which is used to simulate the SB-induced strain concentration behavior.

The reason why we use different slip resistances for the regions inside and outside SB is explained as follows. Based on the SEM and TEM observations in [2.3.3 Microstructure observation](#), for the region outside SB, the RSS is not high enough to let the dislocations cut through γ' phases. So, under the hardening effect induced by γ' phases, the $r_{\text{dislocation}}^s$, $r_{\text{bypassing}}^s$ and r_{lattice}^s are still in action ([Eq. \(11\)](#)). For the region inside SB, the RSS is higher than r_{shear}^s ([Eq. \(13\)](#)). So, the dislocations can shear through γ' phases, and the γ' -associated $r_{\text{dislocation}}^s$, $r_{\text{bypassing}}^s$ do not take effect anymore ([Eq. \(14\)](#)).

It is worth explaining why we use r_{shear}^s as the CRSS of SB initiation ([Eq. \(13\)](#)), but use r_{lattice}^s as the slip resistance in flow rule ([Eq. \(14\)](#)). First, the r_{shear}^s is the threshold that dislocations can observably enter γ' phases, and the SBs can only come into being after $\text{RSS} > r_{\text{shear}}^s$. After SB initiation, the APBs will disappear at inside-SB-region, and the APB-based r_{shear}^s will not take effect anymore. Instead, the SB will open a channel within γ' phase, to make the γ' -associated hardening effects become ineffective ([León-Cázares et al., 2020](#); [Wang et al., 2023](#); [Westbrooke et al., 2005](#)). After that, the dislocations can propagate easily along the SB channels, instead of bypassing γ' phases or piling up at γ/γ' interfaces. So, the γ' -associated $r_{\text{bypassing}}^s$ and $r_{\text{dislocation}}^s$ are not effective anymore inside SB, which is the mechanism of SB-induced strain concentration for SX superalloy. Under this condition, only r_{lattice}^s should be used as the slip resistance in flow rule ([Eq. \(14\)](#)). Besides, the smooth transition from APB-associated r_{shear}^s to SB-associated r_{lattice}^s is not considered in flow rule for the region inside SB, which is a limitation of model.

The components in slip resistance ([Eq.\(11\)](#)) are expressed as follows. The dislocation hardening $r_{\text{dislocation}}^s$ can be expressed by the dislocation density ([le Graverend et al., 2014](#)):

$$r_{\text{dislocation}}^s = \theta \sum_{i=1}^{12} h^{s,i} \rho_{\text{im}}^i \quad (15)$$

where ρ_{im}^i is the density of immobile dislocations stacked at γ/γ' interfaces, $h^{s,i}$ is the component of hardening matrix that captures the interaction of dislocation hardening between different slip systems ([Xiong Yukai, 2023](#); [Zhang et al., 2023b](#)), θ is a constant. Besides, the evolution of dislocation density is given as ([Cormier and Cailletaud, 2010](#); [le Graverend et al., 2014](#)):

$$d\rho_{\text{im}}^s = (1 - a\rho_{\text{im}}^s) d\nu^s \quad (16)$$

where ν^s is the accumulated plastic resolved shear strain in slip system, and a is a constant. Furthermore, the $r_{\text{bypassing}}^s$ can be expressed by the well-known Orowan stress ([le Graverend et al., 2014](#)):

$$r_{\text{bypassing}}^s = \sqrt{\frac{2}{3}} \frac{Gb}{w} \quad (17)$$

where w is the matrix channel width of SX superalloy. For the r_{shear}^s , since the TEM observation shows that the dislocations do not enter the γ' phase in pair, the weak-coupled mechanism is dominant for the shear of γ' phase ([Reed, 2008](#)):

$$r_{\text{shear}}^s = \frac{\gamma_{\text{APB}}}{2b} \left[\left(\frac{6\gamma_{\text{APB}} f_{\gamma'} d_p}{\pi T_d} \right)^{1/2} - f_{\gamma'} \right] \quad (18)$$

where γ_{APB} is the APB energy, $f_{\gamma'}$ is the volume fraction of γ' phase, d_p is the average size of γ' phase, T_d is the line tension of dislocation ([Reed, 2008](#)):

$$T_d = \frac{Gb^2}{2} \quad (19)$$

After that, the simulation method for SB direction is developed as follows. As shown in [Fig. 10](#), a two-dimensional model with a half circular hole is employed in subsequent analysis. As the resolved shear stress at point (x_0, y_0, z_0) near the hole edge meets the criterion of SB initiation ([Eq. \(13\)](#)), the SB comes into being. It should be noted that the judging of SB initiation near hole edge is conducted two times. These two SBs are corresponding to the primary and secondary SBs observed by the experiment. Then, the slip plane Γ^s for the

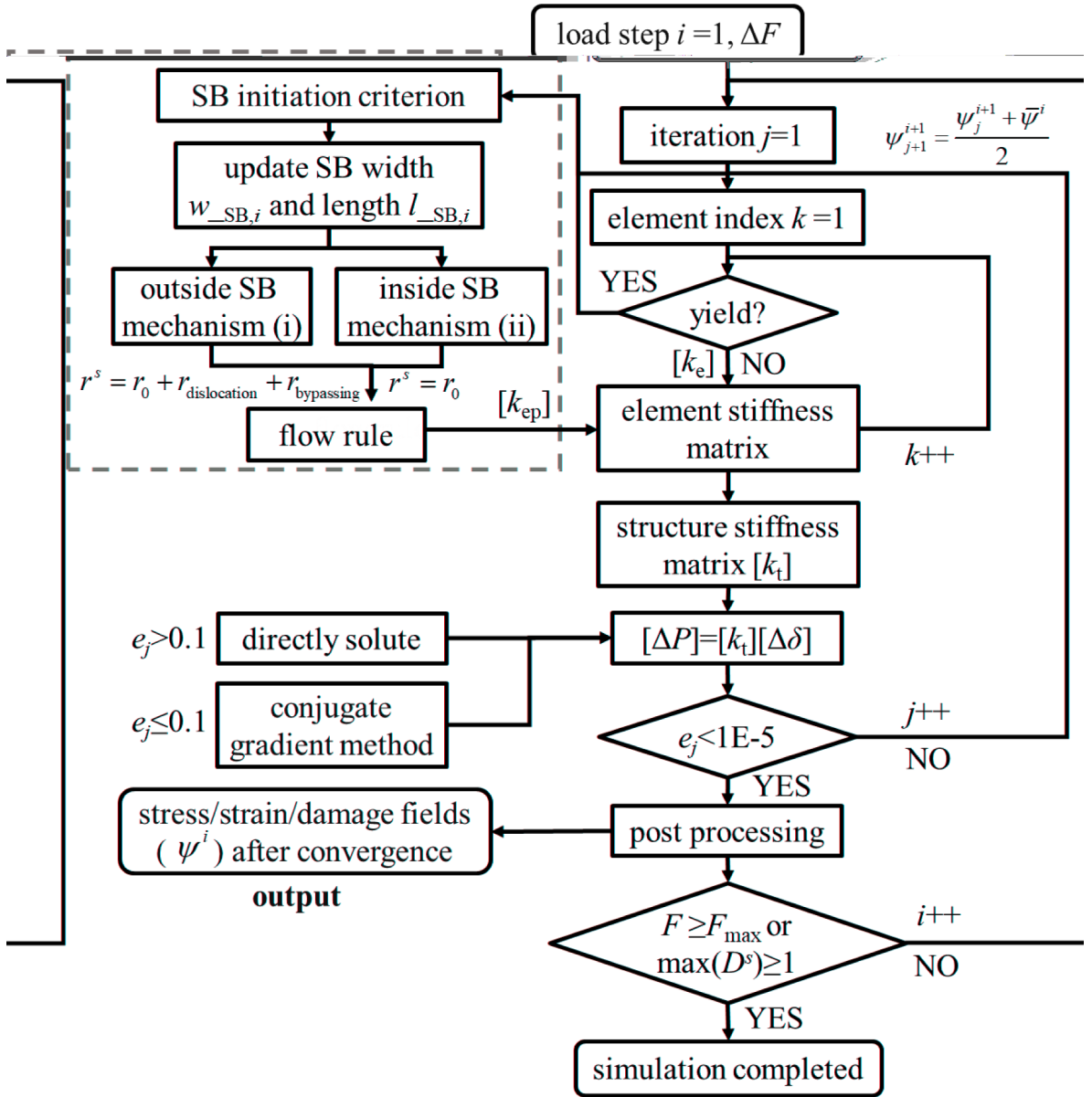


Fig. 11. the flowchart of FE implementation.

activated SB can be determined, and the normal vector of Γ^s in crystal coordinate system can be obtained, which is denoted as $[\vec{m}]_c$. Based on the given primary and secondary orientations of circular hole, the $[\vec{m}]_g$ in global coordinate system can be expressed as:

$$[\vec{m}]_g = [L][\vec{m}]_c \quad (20)$$

where $[L]$ is the coordinate transformation matrix (from crystal to global coordinate system). After that, the analytical equation for crystal plane Γ^s in global coordinate system can be written as:

$$\vec{m}_{g,1}(x - x_0) + \vec{m}_{g,2}(y - y_0) + \vec{m}_{g,3}(z - z_0) = 0 \quad (21)$$

where $\vec{m}_{g,1}, \vec{m}_{g,2}$ and $\vec{m}_{g,3}$ are three components of vector $[\vec{m}]_g$. Under the two-dimensional condition, the component of $\vec{m}_{g,3}(z - z_0)$ can be eliminated. Then, the unit vector $[\vec{v}_{SB}]$ representing the SB direction in global coordinate system can be written as:

$$\left[\vec{v}_{\text{SB}} \right] = \left[\frac{\vec{m}_{g,1}}{\sqrt{\vec{m}_{g,1}^2 + \vec{m}_{g,2}^2}}, \frac{\vec{m}_{g,2}}{\sqrt{\vec{m}_{g,1}^2 + \vec{m}_{g,2}^2}}, 0 \right]^T \quad (22)$$

Furthermore, the simulation method for the evolution of SB width and length is illustrated as follows. It is assumed that the shape of SB remains a rectangle in course of evolution under two-dimensional condition. As shown in Fig. 10, when the resolved shear stress at SB tip (outside SB) reaches the criterion of SB initiation (Eq. (13)), the SB length l_{SB} increases to the corresponding region. As any point at both sides of SB meets the criterion of SB initiation, the w_{SB} becomes higher, and the SB extends to the corresponding region. Under each load step, the extended region of SB is determined using an iterative algorithm, which will be introduced in Section 3.3.

Finally, it is worth explaining the particularity of proposed SB evolution model. For the regions inside and outside SB, the transition of slip resistance (from Eq. (11) to Eq. (14)) is only applicable to SX superalloy with strengthening phases of γ . Because, the framework of this model is established based on the deformation mechanisms (i) and (ii) revealed in 2.3.3 Microstructure observation for SX superalloy, and the expressions of different kinds of slip resistances (from Eq. (15) to Eq. (19)) are derived based on the microstructural features of γ/γ' phases. When generalizing this model to simulate the SB evolution for other materials, the plastic deformation mechanisms and slip resistances need to be re-analyzed.

3.3. FE implementation method

Before applying the proposed SB evolution model on circular hole, the FE implementation method needs to be developed. The CPFE simulation is based on the MATLAB platform ([MathWork](#)). The flowchart of FE implementation is shown in Fig. 11. In general, it is composed of three layers of iteration. The first layer is loop i , which is the iteration of load step. The second layer is loop j , which is to ensure that in each load step, the SB region and stress/strain fields are convergent. The third layer (loop k) is the iteration of element number, which is to construct the stiffness matrix.

For iteration i , the increment is external tensile force. As the external load reaches the pre-defined maximum load, or as the maximum damage among all elements reaches 1, the simulation will be stopped.

For the iteration j , to judge if the simulation is convergent, the residual error e_j is defined as follows:

$$e_j = \frac{\|\Delta\delta_j - \Delta\delta_{j-1}\|}{\|\Delta\delta_{j-1}\|} \quad (23)$$

where $[\Delta\delta]$ is a column vector denoting the increment of displacement for all nodes. To obtain the $[\Delta\delta]$, considering that the structure stiffness matrix is non-singular after applying the boundary condition, the key equation of FE method ($[\Delta P] = [k_t][\Delta\delta]$) can be solved fast and directly by inverting the $[k_t]$ based on MATLAB's on-premise code. This direct solving method is effective only as $e_j > 0.1$. When $e_j \leq 0.1$, the conjugate gradient method is utilized to conduct the iterative solution. Meanwhile, the transfer of physical quantities in adjacent two iterations j is written as:

$$\psi_{j+1}^{i+1} = \frac{\psi_j^{i+1} + \bar{\psi}^i}{2} \quad (24)$$

where ψ_j^i denotes the set of all physical quantities in load step i and sub-step j , and $\bar{\psi}^i$ is the convergent physical quantities in load step i . Eq.(24) is employed to solve the evolution of SB region (Eq.(22)), flow rule (Eq.(10)), slip resistance (Eq. (11)), etc. Besides, to ensure that the simulated SB evolution is convergent, the SB length and width are updated based on ψ_{j+1}^{i+1} in each round of j iteration. The elements at the tip and both sides of SB are enumerated to judge if they meet the criterion of SB initiation (Eq.(13)). If yes, the SB will extend to the corresponding regions.

In iteration k , regarding the proposed flow rule (Eq.(10)), the derivation of stiffness matrix $[k_{\text{ep}}]$ for the yield element is the most critical step (marked as a dotted square in Fig. 11). The $[k_{\text{ep}}]$ is derived as follows. For the yield elements, under the assumptions of small deformation and non-rotation of lattice (Han et al., 2005; Vattré et al., 2014), the Lagrange elastic-plastic strain tensor can be divided into elastic and plastic parts:

$$d[\varepsilon_{\text{ep}}]_g = d[\varepsilon_e]_g + d[\varepsilon_p]_g \quad (25)$$

where $[\varepsilon_{\text{ep}}]_g$, $[\varepsilon_e]_g$ and $[\varepsilon_p]_g$ are the elastic-plastic, elastic and plastic strain tensors in globe coordinate system. The elastic constitutive relationship for SX superalloy can be written as:

$$[\sigma]_g = [D_e]_g [\varepsilon_e]_g \quad (26)$$

where $[D_e]_g$ is the elastic constant matrix in global coordinate system. For the anisotropic SX superalloy with FCC lattice, there are three symmetrical planes of elasticity (Reed, 2008). In the crystal coordinate system, it can be derived that the elastic constant matrix $[D_e]_g$ of SX superalloy contains three independent elastic constants (Li et al., 2022b; Reed, 2008; Ren et al., 2021):

$$[D_e]_c = \begin{bmatrix} 1/E_{[100]} & -\mu_{[100]}/E_{[100]} & 0 \\ -\mu_{[100]}/E_{[100]} & 1/E_{[100]} & 0 \\ 0 & 0 & 1/G_{[001]} \end{bmatrix}^{-1} \quad (27)$$

where $E_{[100]}$, $\mu_{[100]}$ and $G_{[100]}$ are the elastic module, Poisson's ratio, and shear module for [100] orientation of SX superalloy. Based on the coordinate transformation, the elastic constant matrix in global coordinate system can be written as:

$$[D_e]_g = [M]_c [D_e]_c [M]_c^{-1} \quad (28)$$

where $[M]_c$ is a transformation matrix that can be expressed by $[L]$ in Eq. (20). Furthermore, the right side of Eq.(25) can be expressed using stress tensor:

$$d[\varepsilon_{ep}]_g = ([D_e]_g^{-1} + [D_p]_g^{-1}) d[\sigma]_g \quad (29)$$

where $[D_p]_g$ is a plastic constant matrix. To derive the $[D_p]_g$ in Eq.(29), based on Eq.(10), the relationship between the increments of resolved shear stress and strain can be expressed as:

$$d[\gamma^s] = [K] d[\tau^s] \quad (30)$$

where $[K]$ is a square matrix with a size of 12×12 . The non-zero components only appear on the diagonal, which can be expressed based on the flow rule (Eq. (10)):

$$K_{s,s} = \frac{d\gamma^s}{d\tau^s} = \left(\frac{|\bar{\tau}^s| - r^s}{\tau_0} \right)^n \frac{1}{(1 - D^s)} \left(\tau^s \geq r^s \right) \quad (31)$$

where $K_{s,s}$ denotes the component of $[K]$ matrix on row s and column s . For the slip system where $\tau^s < r^s$, the $K_{s,s}$ equals 0. Meanwhile, based on Eq. (4) and Eq. (3), the relationships between resolved shear stress/strain and stress/strain tensors in crystal coordinate system can be written as:

$$\begin{cases} d[\tau^s] = [T_0] d[\sigma]_c \\ d[\varepsilon_p]_c = [T_1] d[\gamma^s] \end{cases} \quad (32)$$

where $[T_0]$ and $[T_1]$ denote the coordinate transformation matrices. These two matrices can be derived based on the $[P^s]$ in Eq. (5). For two-dimensional condition, these two tensors are explicitly given as follows:

$$\begin{aligned} [T_0] &= \frac{1}{\sqrt{6}} \begin{pmatrix} 1 & -1 & 0 & 0 & 1 & -1 & 1 & -1 & 0 & 0 & 1 & -1 \\ 0 & 1 & -1 & 1 & -1 & 0 & 0 & 1 & -1 & 1 & -1 & 0 \\ 1 & 0 & -1 & -1 & 0 & 1 & 1 & 0 & -1 & -1 & 0 & 1 \end{pmatrix}^T [T_1] \\ &= \frac{1}{2\sqrt{6}} \begin{pmatrix} 2 & -2 & 0 & 0 & 2 & -2 & 2 & -2 & 0 & 0 & 2 & -2 \\ 0 & 2 & -2 & 2 & -2 & 0 & 0 & 2 & -2 & 2 & -2 & 0 \\ 1 & 0 & -1 & -1 & 0 & 1 & 1 & 0 & -1 & -1 & 0 & 1 \end{pmatrix} \end{aligned} \quad (33)$$

Substituting Eq. (33) into Eq. (32), the relationship between stress and strain tensors in crystal coordinate system can be expressed as:

$$d[\varepsilon_p]_c = [T_1] [K] [T_0] d[\sigma]_c \quad (34)$$

Further, the relationship between the increments of stress and strain tensors in global coordinate system can be written as:

$$d[\varepsilon_p]_g = [L]^{-1} [T_1] [K] [T_0] [L] d[\sigma]_g \quad (35)$$

Therefore, by comparing Eq. (29) and Eq. (35), the $[D_p]_g$ can be obtained as:

$$[D_p]_g = ([L]^{-1} [T_1] [K] [T_0] [L])^{-1} \quad (36)$$

Since the $[K]$ in Eq. (31) changes with the load step, the $[D_p]_g$ is not a constant matrix. Based on Eq. (36) and Eq. (28), Eq.(29) can be re-written as:

$$d[\sigma]_g = ([D_e]_g^{-1} + [D_p]_g^{-1})^{-1} d[\varepsilon_{ep}]_g \quad (37)$$

The above equation explicitly expresses the relationship between the increments of stress and strain tensors. Meanwhile, the definition of $[D_{ep}]_g$ is as follows:

Table 3

the calibrated parameters used in CPFE simulation

symbol	physical meaning	value	unit
f_γ	volume fraction of γ phase	0.71	dimensionless
d_p	average size of γ phase	366	nm
w	matrix channel width for γ phase	50	nm
b	norm of burgers vector	0.255	nm
γ_{APB}	anti-phase energy	0.06 (RT) / 0.062 (760°C) / 0.065 (850°C) / 0.04 (980°C)	J
a	coefficient in dislocation density evolution	76	dimensionless
θ	coefficient in dislocation hardening	300	MPa
$[h]$	hardening matrix	0.07-0.625	dimensionless
$E_{[001]}$	elasticity modulus of [001] orientation	120 (RT) / 108 (760°C) / 101 (850°C) / 91 (980°C)	GPa
$\mu_{[100]}$	Poisson's ratio of [001] orientation	0.361 (RT) / 0.402 (760°C) / 0.412 (850°C) / 0.425 (980°C)	dimensionless
$G_{[100]}$	shear modulus of [001] orientation	71 (RT) / 57 (760°C) / 53 (850°C) / 46 (980°C)	GPa
r_s^s	lattice resistance	135 (RT) / 137 (760°C) / 175 (850°C) / 33 (980°C)	MPa
n	exponent in flow rule	1.25	dimensionless
τ_0	coefficient in flow rule	3.5×10^4	MPa
W_{cr}	critical plastic work density in slip system	195	MPa

$$d[\sigma]_g = [D_{ep}]_g d[\varepsilon_{ep}]_g \quad (38)$$

By comparing Eq. (37) and Eq. (38), the expression of $[D_{ep}]_g$ can be obtained as:

$$[D_{ep}]_g = \left([D_e]_g^{-1} + [D_p]_g^{-1} \right)^{-1} \quad (39)$$

Finally, based on the $[D_{ep}]_g$ in Eq. (39), the $[k_{ep}]$ for yield element can be expressed as:

$$[k_{ep}] = \int \int_{\Omega} [B]^{-1} [D_{ep}]_g [B] t dx dy \quad (40)$$

where $[B]$ is the geometry matrix, Ω denotes the area of element in global coordinate system, and t is the thickness of the two-dimensional element. Eq. (40) can be solved based on the method of Gauss quadrature.

3.4. Parameters calibration and FE model

First, some microstructural parameters in proposed model can be determined directly. For the SX superalloy used in this study, the volume fraction and average size of γ phase, matrix channel width of γ phase can be measured directly. The norm of Burgers vector for the FCC lattice can also be measured by the diffraction pattern of TEM. Besides, the energy of anti-phase boundary is determined by classic literature (Reed, 2008). The parameters in dislocation hardening and evolution of dislocation density are referred to previous works (Guo et al., 2021a; le Graverend, 2019; le Graverend et al., 2014; Zhang et al., 2023b). The calibrated microstructure-sensitive parameters are listed in rows 1 to 8 of Table 3.

Secondly, the parameters of mechanical properties can be obtained from the material data book. For the SX superalloy used, all the elasticity parameters at different temperatures can be found in a material data book (Huichen Yu, 2010). Regarding the components of slip resistance shown in Eq. (11), $r_s^s_{\text{dislocation}}$ and $r_s^s_{\text{bypassing}}$ have already been determined by the microstructural parameters. Derived from Eq. (11), the r_s^s lattice is calibrated based on the yield stress for the tension of [001] orientation:

$$r_s^s_{\text{lattice}} = P' \sigma_y^{[001]} - r_s^s_{\text{dislocation}} - r_s^s_{\text{bypassing}} \quad (41)$$

where $\sigma_y^{[001]}$ is the yield stress (0.2% plastic strain) of SX superalloy under the tension of [001] orientation, and P' is an orientation-dependent Schmid factor. Since the temperature effect is studied in this work, the temperature-varying $\sigma_y^{[001]}$ with 0.2% plastic strain is the only yield data that can be found from reference (Huichen Yu, 2010). The use of $\sigma_y^{[001]}$ at 0.2% plastic strain is an approximation. The error of this approximation is quantified as follows. As shown in Fig. 4 (a), for NH1-RT without hole, the plasticity first appears at data point #1 at the earliest situation. The $\sigma_y^{[001]}$ at point #2 is close to #1. The upper limit of error is marked as $\Delta\sigma=21$ MPa, and the error of RSS should be as low as 8.6 MPa after considering Schmid factor. Besides, the upper limit of relative error is as low as 2.3%. Thus, this approximation is relatively reasonable for the SX superalloy used in this work. It should be noted that the condition for Eq. (41) to hold is that SB has not initiated at 0.2% plastic strain. The DIC results of NH1-RT (the primary orientation is close to [001]) are used to prove this. The data points #2 and #3 corresponding to $\sigma_y^{[001]}$ and SB initiation are marked in Fig. 4 (a). It can be seen that SB initiates at #3 point with $\bar{\epsilon} \approx 2\%$, which is far away from #2 point (0.2% plastic strain). The calibrated parameters corresponding to the mechanical properties can be found in rows 9 to 12 of Table 3.

Other parameters are calibrated by the measured stress-strain curve. The n , τ_0 in flow rule (Eq.(10)) and W_{cr} in damage evolution (Eq. (7)) are only three parameters that are determined by fitting the test data of NH1. First, based on the measured stress and strain inside SB (the corresponding region is shown in the bottom right corner of Fig. 12 (b)), the W_{cr} is obtained by integrating the resolved

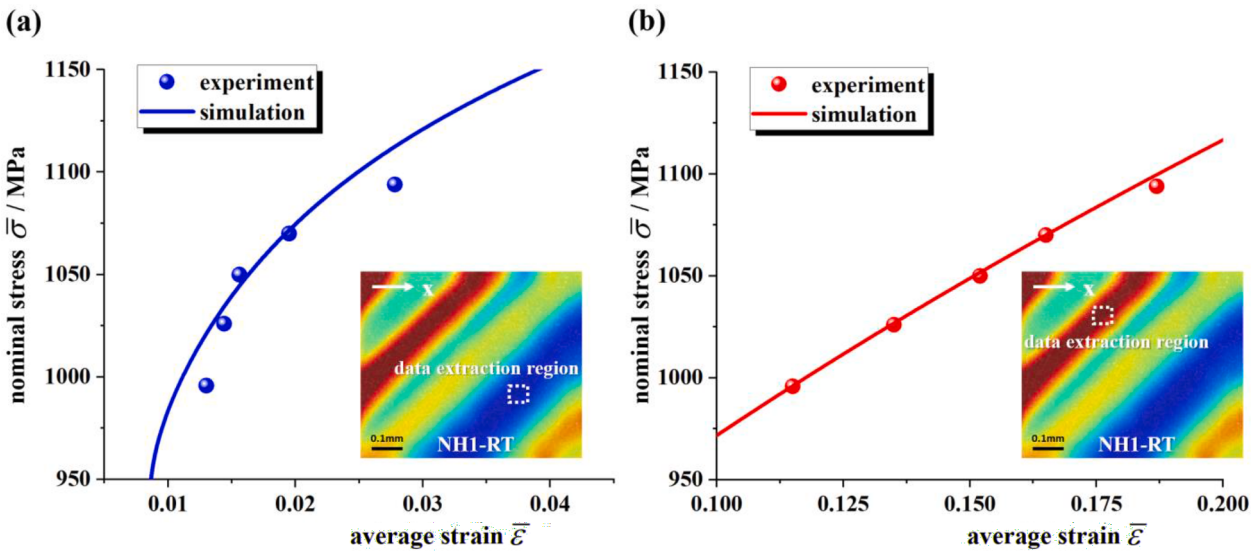


Fig. 12. parameter calibration for the n and τ_0^s in flow rules using the test data of NH1-RT: (a) stress and strain outside SB; (b) stress and strain inside SB.

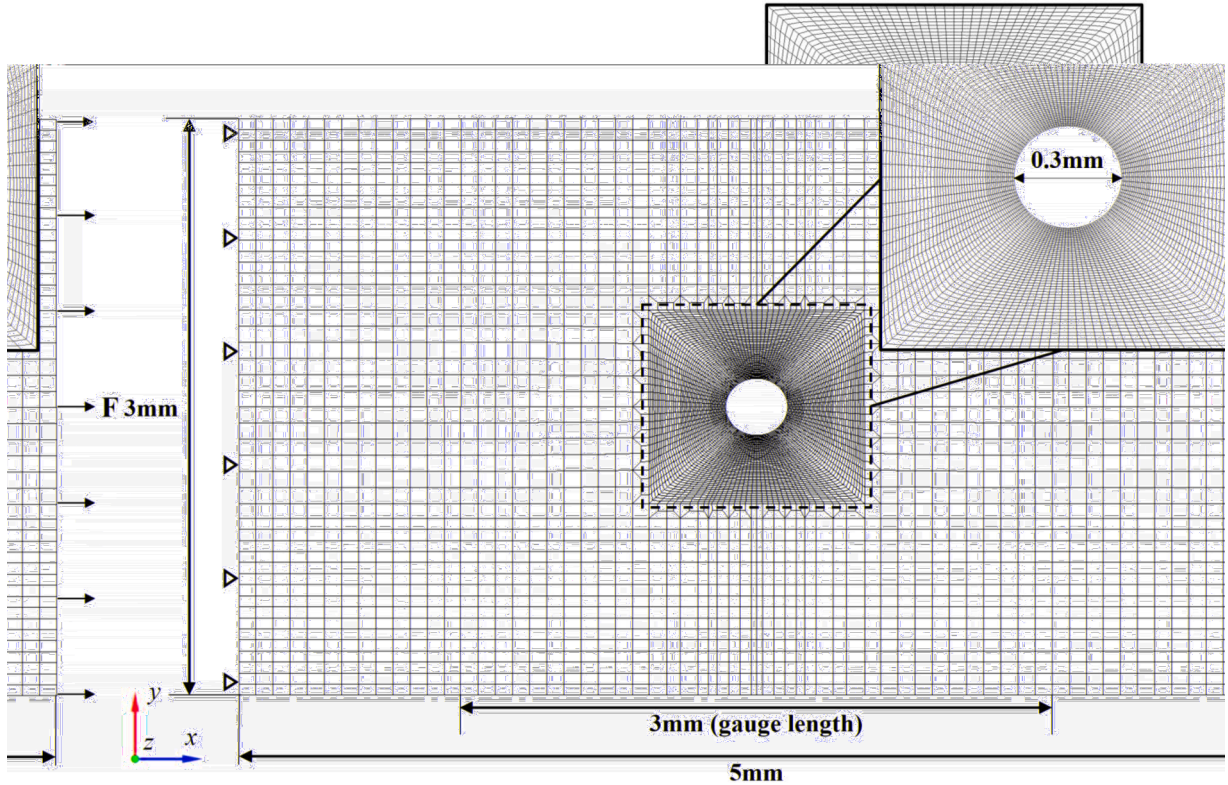


Fig. 13. FE model for the specimen with circular hole.

shear stress and strain along the load path for the slip system of activated SB:

$$W_{cr} = \int \tau^s d\gamma^s = \sum_{i=1}^n \tau_i^s \Delta \gamma_i^s \quad (42)$$

where n denotes the number of data points. For above equation, the starting point of integration is the initiation of plasticity, and the end of integration is when the microcrack nucleation can be observed. Meanwhile, taking W_{cr} and evolution of D^s as known quantities, the n and τ_0 are calibrated by fitting the stress and strain curve. The least square method is employed to optimize the values of n and τ_0 . It should be noted that the optimized values of n and τ_0 are unique. As shown in Fig. 12, for the region inside and outside SB, the evolution of stress and strain can be well described by the rate-independent flow rule after the parameter optimization. Their values are listed in the last three rows of Table 3.

To validate the proposed model, the CPFE computations are conducted under experimental conditions. As shown in Fig. 13, a two-dimensional FE model with a size of $3\text{mm} \times 5\text{mm}$ is established for the specimen used in the experiment. The region within the gauge length of 3mm is involved in the FE model. In this simulation, we focus on the SB evolution behavior near circular hole. So, we use refined meshes at the region ($1\text{mm} \times 1\text{mm}$) near circular hole to achieve the high resolution of stress and strain distributions. Meanwhile, to save the computation cost, we use coarse meshes in the region away from circular hole. It should be noted that the simulation of SB-induced strain concentration is also performed at the region with coarse meshes. Although the fidelity or resolution of stress and strain distributions at the region with coarse meshes are not high, this limited fidelity has little effect on the simulation results at the region with refined meshes, which can be proved in Appendix A. The regions with refined and coarse meshes contain 5800 and 2932 elements, respectively, which can pass the mesh size independence check (Appendix A). The element type is planar four-node quadrilateral without mid-node. The displacement constraint $\delta_x=0$ is applied to the left boundary of the FE model. Meanwhile, the tensile force is applied to the right boundary of the FE model along x direction. The simulation involves more than 50 load steps in total.

4. Comparisons and discussions

In this section, the test results are utilized to validate the model, regarding stress-strain curves, strain distributions, and SB evolution. Then, a comparison is made between the conventional and proposed models. Finally, some possible causes of relative errors between experiment and simulation are discussed.

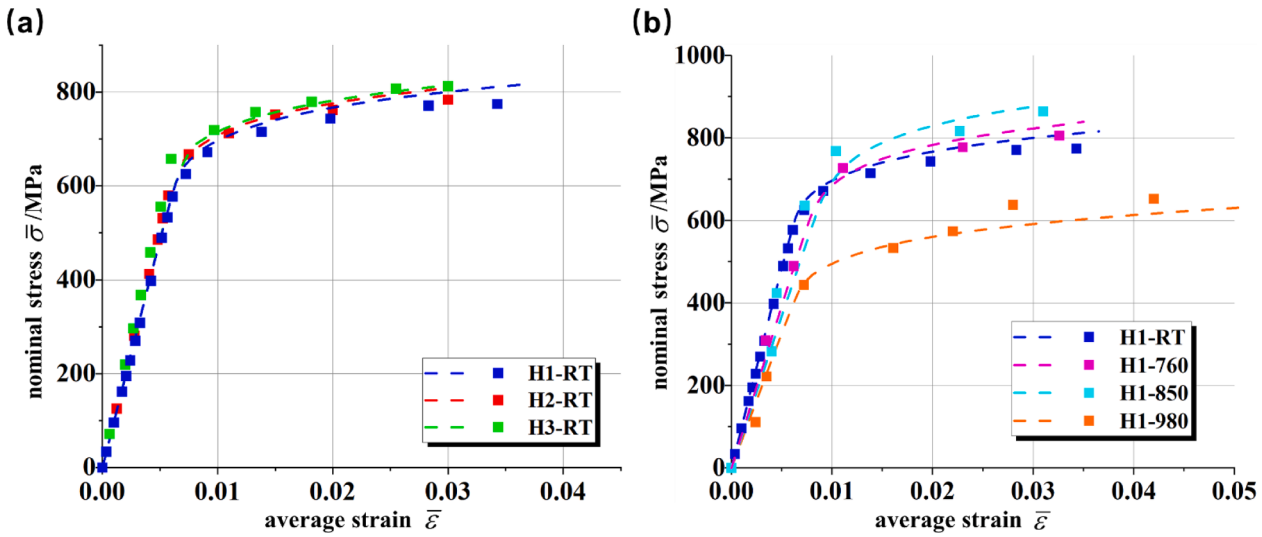


Fig. 14. comparisons of stress-strain curves between simulation and experiment: (a) at different secondary orientations; (b) at different temperatures.

Table B.1
calibrated parameters in Ramberg-Osgood formula

		E / GPa	K / MPa	n / dimensionless	yield stress / MPa
simulation	H1-RT	102	1058	0.0733	670
	H2-RT	100	1047	0.0659	675
	H3-RT	101	1046	0.0678	686
	H1-760	80.8	1113	0.0765	691
	H1-850	74.3	1176	0.0735	744
	H1-980	70.1	854	0.0952	472
experiment	H1-RT	94.3	957	0.0570	672
	H2-RT	92.7	922	0.0424	703
	H3-RT	111	1022	0.0600	710
	H1-760	89.5	1003	0.0589	695
	H1-850	98.3	1182	0.0828	710
	H1-980	64.9	1086	0.1424	448

4.1. Comparisons between experiment and simulation

The measured stress-strain curves shown in Section 2.3.1 are employed to validate the simulation results. As shown in Fig. 14 (a), the stress-strain curves for H1, H2, H3 are nearly coincident. Meanwhile, Fig. 14 (b) indicates that the yield stress and ultimate tensile strength are the highest at 850°C, and lowest at 980°C. The simulated stress-strain curves accurately reflect the observed trends in the experiment. Besides, the yield stress and $\bar{\epsilon}$ at microcrack nucleation in simulation and experiment are compared as follows. To determine the yield stress, the Ramberg-Osgood formula is employed to fit the data points (Ramberg and Osgood, 1943). The calibrated parameters for both simulation and experiment are listed in Table B.1. The details of parameter determination are illustrated in Appendix B. Since the damage evolution is considered in Eq.(7), the proposed model can predict the microcrack nucleation.

The simulation can effectively capture the variation trend of $\bar{\epsilon}$ at microcrack nucleation under different temperatures and secondary orientations (H1-980>H1-RT>H1-760>H1-850>H2-RT≈H3-RT). Meanwhile, the nominal stress corresponding to 0.2% plastic strain is determined as yield stress. The variation trend of yield stress (H1-850>H3-RT>H2-RT>H1-760>H1-RT>H1-980) can also be effectively predicted by proposed model. The root-mean-square error (RMSE) is employed to quantify the accuracy of simulation:

$$\text{RMSE} = \sqrt{\frac{\sum_{i=1}^m (v_s^i - v_e^i)^2}{m}} \quad (43)$$

where v_s and v_e are the values of physical quantities for simulation and experiment, and m is the quantity of data points. The RMSEs are 23.6 MPa and 3.57% for the prediction of yield stress and $\bar{\epsilon}$ at microcrack nucleation.

The evolution of strain distribution measured by DIC is utilized to validate the simulation result. As shown in Fig. 15, to quantify the direction of SB, a parameter α is defined as the angle between SB and horizontal direction. As discussed in Section 2.3.2, the secondary orientation has a significant effect on the direction of SB. As shown in the first row of Fig. 15, in the case of H1 specimen, the SBs at both sides of circular hole are roughly symmetrical, while the SBs exhibit asymmetry in the case of H2 and H3. This difference is associated with the distribution of maximum resolved shear stress (MRSS) near hole edge. For H1 specimen, the regions with higher MRSS are symmetrical with respect to the straight line of $\alpha=0^\circ$, while the MRSS concentrates at the right side of a straight line with $\alpha=0^\circ$ for H2 and H3. As shown in the second row of Fig. 15, the simulation can effectively predict the distribution of SB direction at different secondary orientations, and the primary and secondary SBs can be simulated. The RMSE for the prediction of α is 4.0° .

Furthermore, to quantitatively compare the strain distribution, a circular path A (twice the diameter of hole) is defined (see the left-top corner of Fig. 15). The strain distributions along path A are extracted and filtered. As shown in the third row of Fig. 15, the curves are relatively stable before the SB initiation. After the initiation of SBs, two peaks can be found along path A, which is caused by the strain concentration inside SBs. For the H1 specimen, these two SBs have almost the same degree of strain concentration, while the strain concentrates more heavily at the primary SB for the H2 and H3. Regarding this strain concentration behavior, the simulation results are consistent with those of experiment in terms of tendency.

The observed SB width evolution behavior is used to validate the simulation results. It should be noted that the SB width in experiment is measured by comparing strain distribution (along path A) with the average strain $\bar{\epsilon}$, which is shown in the second row and third column of Fig. 15. As shown in Fig. 16 (a), in the case of H1-RT, two SBs nucleate simultaneously, and their widths are close during evolution. For the H2-RT and H3-RT (Fig. 16 (b) and (c)), the primary SB nucleates earlier than the secondary SB, and the width of primary SB is much larger than that of secondary SB. This is caused by the difference of MRSS distributions near hole edge. The location with higher MRSS corresponds to higher SB width and evolution rate. The SB widths for H1, H2, and H3 all increase with nominal stress. Besides, as shown in Fig. 16 (d), temperature has significant effects on the critical nominal stress of SB initiation. The SB evolves earliest for H1-980, and latest for H1-850, which is induced by the difference of γ_{APB} . Besides, there is no significant change for the magnitude of SB width at different temperatures. The simulation can effectively describe these trends. For all above comparisons between simulation and experiment, the RMSE is 0.038 mm for the prediction of SB width.

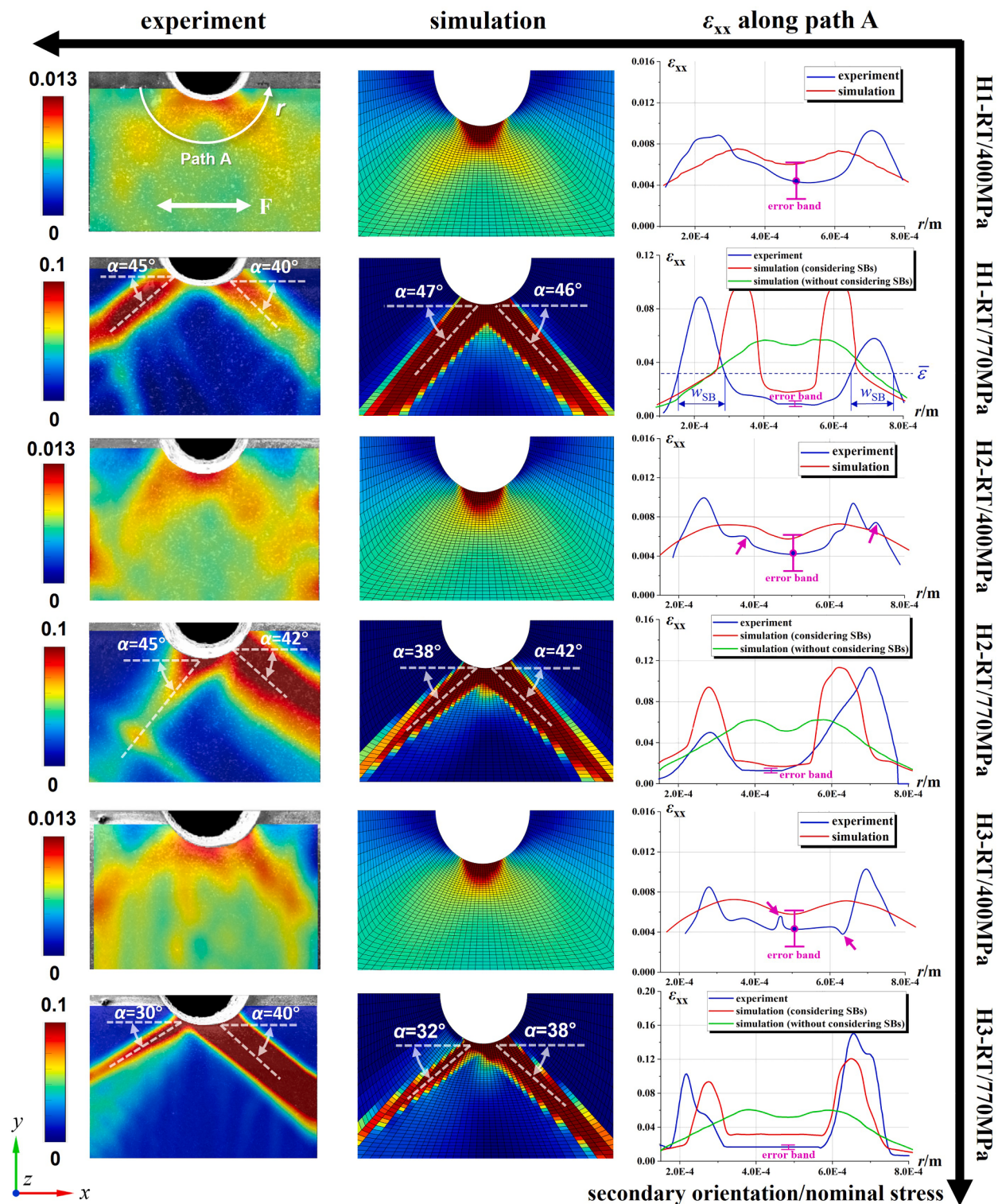


Fig. 15. Comparisons of total strain (ϵ_{xx}) distributions between experiment and simulation at different secondary orientations.

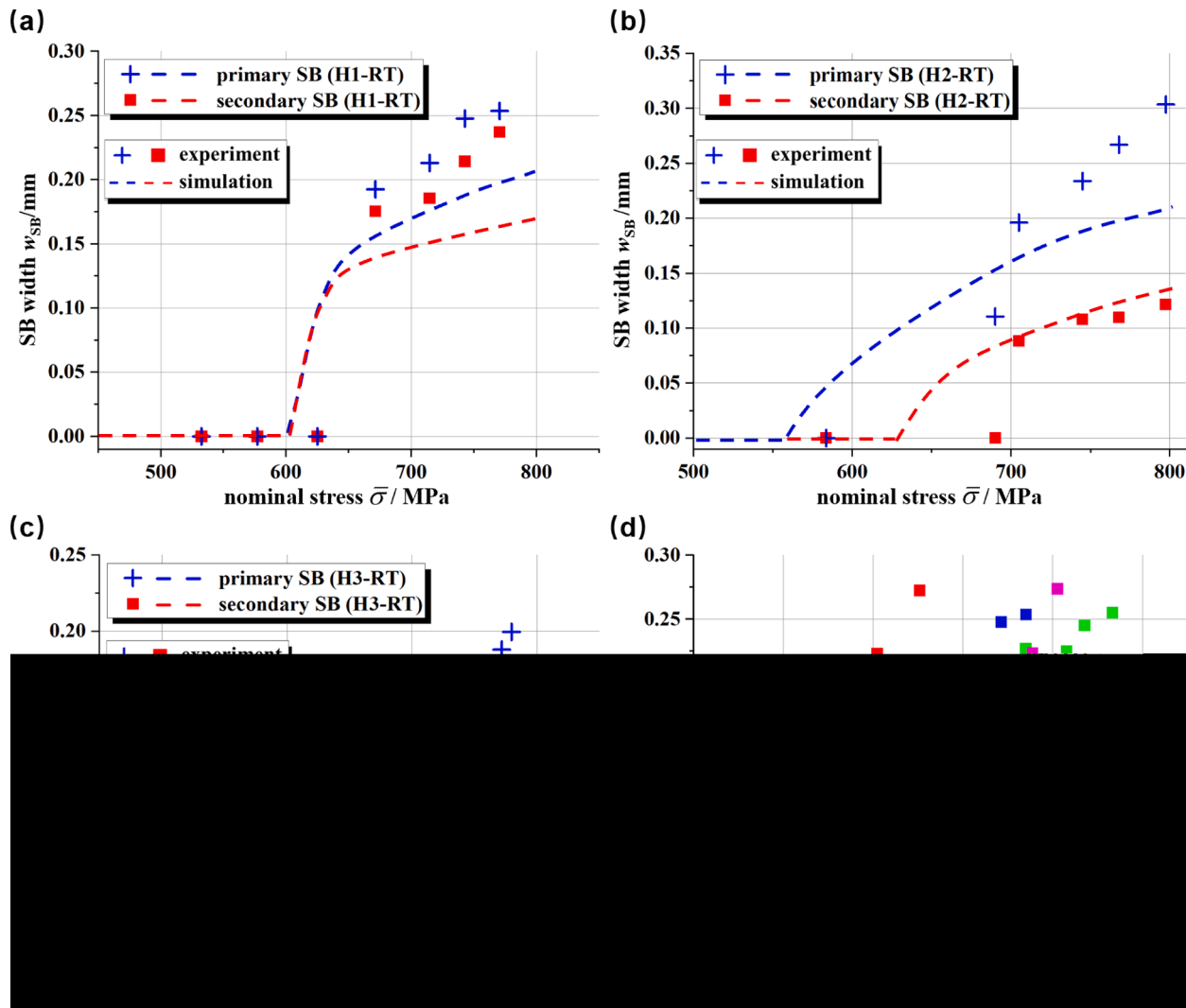


Fig. 16. comparisons between simulation and experiment for SB width evolution: (a) H1-RT; (b) H2-RT; (c) H3-RT; (d) H1-RT / H1-760 / H1-850 / H1-980.

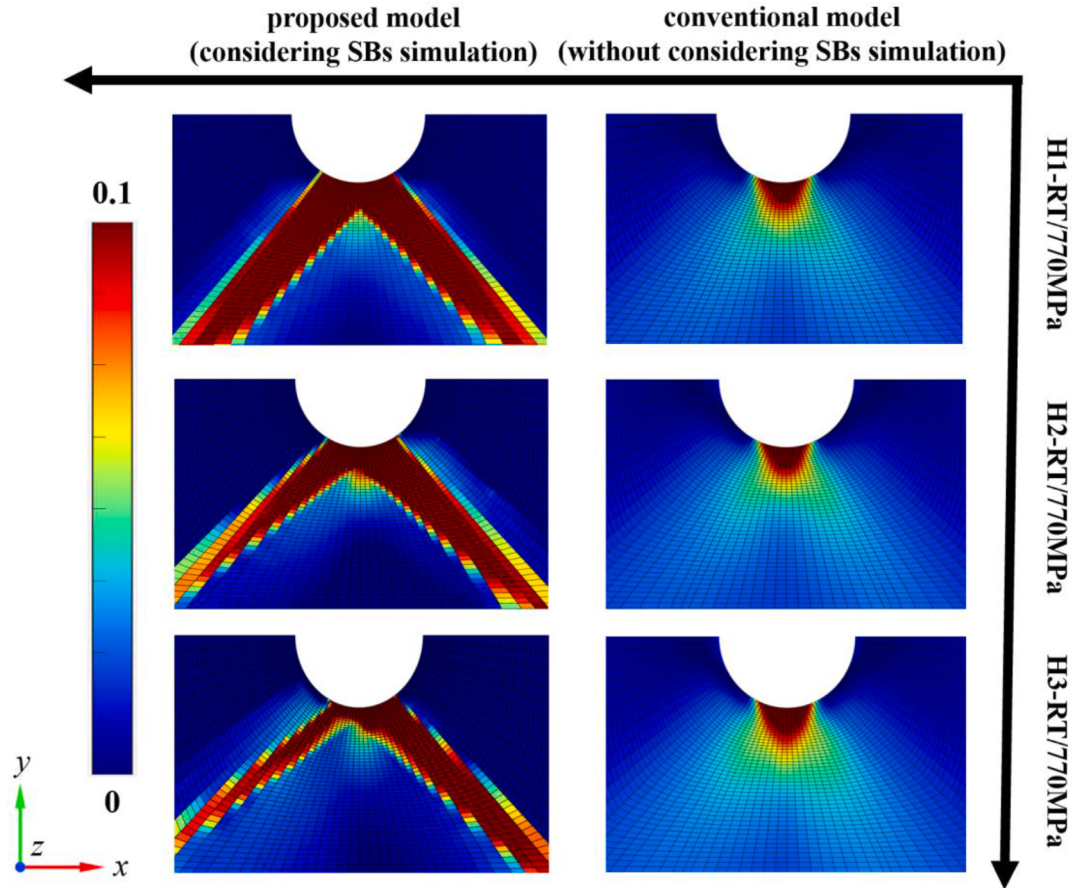


Fig. 17. comparisons of total strain (ϵ_{xx}) distributions between proposed model and conventional method at different secondary orientations.

4.2. Comparisons between conventional model and proposed model

For purpose of comparison, the conventional model is utilized to conduct the simulation under the same load condition. In conventional model, the deformation mechanism (ii) and SB evolution are not considered. All the elements have the same flow rule (without considering the transformation of slip resistance after SB initiation).

The other computation settings are the same as those of proposed model. The simulation results are shown in Fig. 17. For conventional model, the strain distributions are roughly symmetrical. The secondary orientation has a slight effect on the strain distribution and magnitude. Compared with the proposed model, the conventional model cannot simulate the primary and secondary SBs, and fails to describe the change of SB direction and strain concentration degree in different secondary orientations. Moreover, the strain distributions along path A for conventional model are plotted in the last column of Fig. 15. The conventional model cannot effectively describe the SB-induced strain concentration behavior and has lower accuracy than the proposed model.

4.3. Discussions on the relative errors between experiment and simulation

Based on the comparisons between experiment and simulation, there are some relative errors in the proposed model. The possible causes of relative error are discussed in the aspects of experiment and simulation.

Some deviations from the ideal state in the experiment could contribute to relative errors. First, some small misorientations existing in the as-received SX superalloy could influence the direction of SB. The probability density distribution of misorientation is shown in Fig. 18 (a). Although most of the misorientations are below 0.5° , some of them ranging from 0.5° to 2.5° will partly influence the SB direction. Secondly, the defects at hole edge could influence the SB evolution. Some dendrites, eutectics, or irregular geometry caused by processing technology could lead to the stress concentration and accelerate the SB evolution. This can explain why the SB widths in experiments are mostly higher than those in simulation. Thirdly, the error of DIC measurement could contribute to the relative error of strain distribution. The random error of DIC measurement under SEM is shown in Fig. 18 (b), which is obtained by postprocessing two speckle patterns with translation transformation only. This error is induced by noise and distortion during SEM imaging and has the same magnitude as the relative error shown in Fig. 15, especially for the comparisons under 400 MPa.

As shown in the third column of Fig. 15, it is worth explaining why the relative error at 400 MPa is larger than that at 770 MPa. The

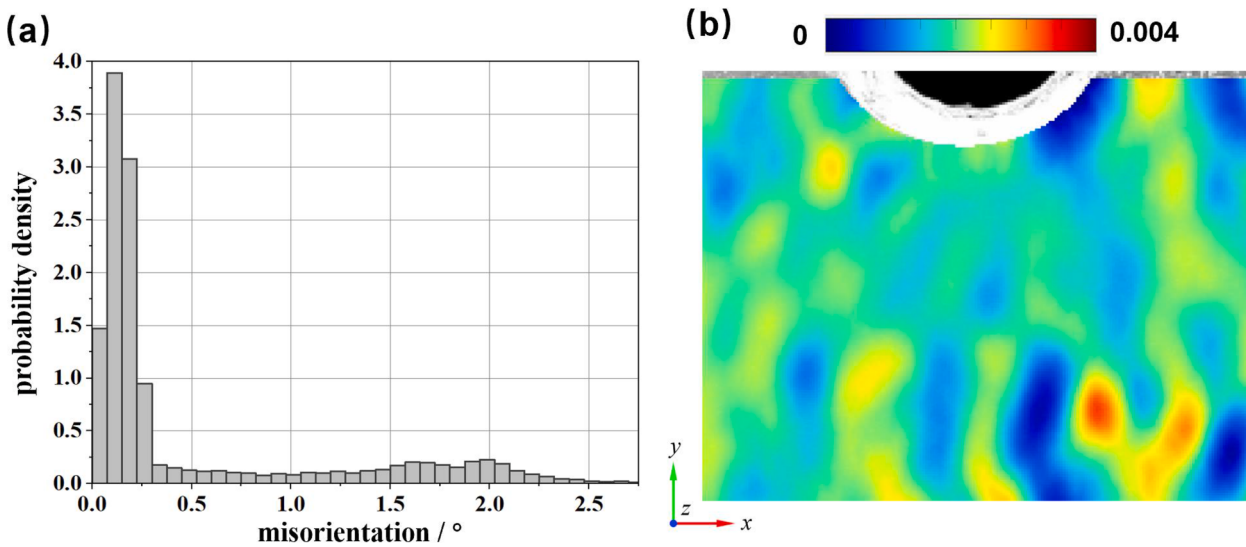


Fig. 18. some possible causes of relative error between experiment and simulation: (a) probability density distribution of misorientation; (b) absolute value of DIC random error for ϵ_{xx} .

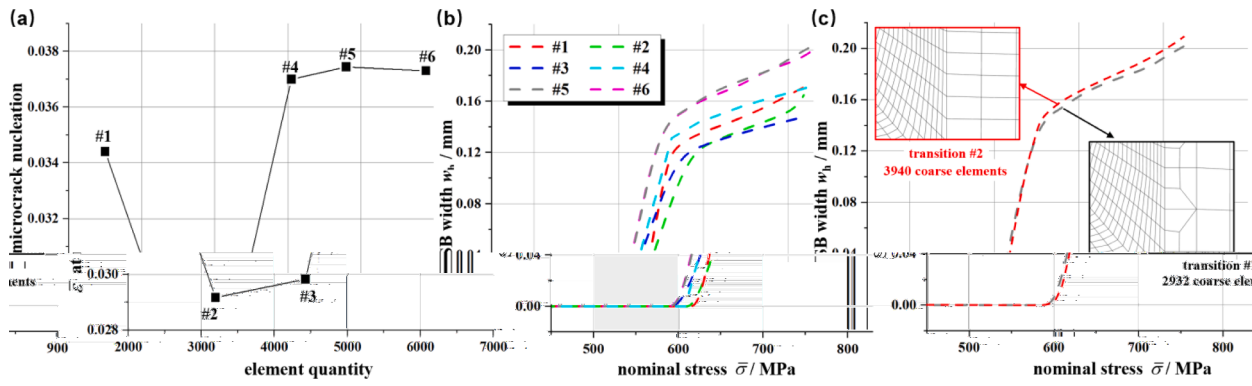


Fig. A1. results of mesh size independence check: (a) ε at microcrack nucleation under different element quantities for the side with refined meshes; (b) SB width evolution under different element quantities for the side with refined meshes; (c) SB width evolution under different element quantities for the side with coarse meshes.

misorientation and defect mentioned above could equally have contributed to the relative errors at 400 MPa and 770 MPa. But the random error of DIC has a greater impact on the relative error at 400 MPa before SB initiation. The explanations are as follows. First, the random error of DIC is induced by the noise and distortion during SEM imaging process. The magnitude of DIC random error does not change with load level, which could have the same absolute values at 400 MPa and 770 MPa. Meanwhile, the scale of vertical axis at 400 MPa is about 10 times smaller than that at 770 MPa. So, as marked in the third column of Fig. 15 using error band, the unchanged random error plays a more important role at 400 MPa. As marked with pink arrows in third column of Fig. 15, some randomly localized peaks can be found along path A, and the localized peak disappears at 770 MPa, which also indicates that the random error of DIC has greater influence at 400 MPa.

At last, there are some limitations in the proposed model, which could result in more obvious relative error at 400 MPa before SB initiation. Because, more complex and intercoupled hardening mechanisms including dislocation hardening, dislocation bypassing, and lattice resistance take effect before SB initiation. These limitations can be listed as follows. (1) The flow rule in proposed model is based on rate-independent plasticity. The viscoplasticity is not considered, which could have more effect before SB initiation (Li et al., 2020; Zhou et al., 2019). (2) The flow rule with power law is semi-empirical, which is not based on the Orowan equation that can capture more details of dislocation motion (Zhang et al., 2023a). (3) Under various mechanisms of dislocation motion before SB initiation, the nonlocal effect and dislocation flux cannot be captured by the CP framework used in this work (Xiong Yukai, 2023; Zhang et al., 2023b). Regarding all above defects, we will take efforts to improve this model in the future.

5. Conclusions

In this study, regarding the SB evolution behavior near circular hole, the experiment and simulation investigations are conducted. In-situ tensile tests combined with DIC technique are conducted on specimens with circular hole, to characterize the SB evolution at different secondary orientations and temperatures. A mechanism-based SB evolution model is proposed to capture the SB initiation/evolution, SB direction, SB-induced strain concentration, and microcrack nucleation of circular hole.

In experimental part, the conclusions can be drawn as follows.

- (1) At the macro level, the temperature has a significant effect on stress-strain curves of specimens with circular holes, while the secondary orientation has less effect.
- (2) The DIC measurement indicates that the strain concentrates at SB. There are primary and secondary SBs near hole edge. The degree of strain concentration is higher in primary SB, and lower in secondary SB.
- (3) Secondary orientation has a great impact on SB direction, while temperature significantly influences the critical nominal stress of SB initiation.
- (4) The microstructure observation indicates that γ phases are sheared and lose the ability to impede the dislocations inside SB, which induces the strain concentration and microcrack nucleation inside SB.

Regarding the simulation part, the following conclusions are drawn.

- (1) The proposed model can effectively describe the stress-strain curves of the specimen with circular hole. Meanwhile, the variation trends of yield stress ($RMSE=23.6\text{MPa}$) and $\bar{\varepsilon}$ at microcrack nucleation ($RMSE=3.57\%$) under different temperatures and secondary orientations can also be effectively predicted.
- (2) Based on the proposed SB evolution model, the SB initiation, direction and width evolution for both primary and secondary SBs can be effectively simulated, with RMSEs are 4.0° for SB direction and 0.038 mm for SB width.
- (3) Compared with the conventional model, the proposed model has ability to simulate the direction and strain concentration of primary and secondary SBs.

CRediT authorship contribution statement

Zixu Guo: Methodology, Conceptualization, Software, Data curation, Writing – original draft, Formal analysis, Investigation. **Ziyuan Song:** Writing – original draft, Formal analysis, Investigation. **Xin Ding:** Software, Data curation. **Kaimin Guo:** Formal analysis, Investigation. **Hongzhuo Liu:** Writing – original draft, Formal analysis. **Han Yan:** Methodology, Investigation. **Dawei Huang:** Writing – review & editing, Investigation, Supervision, Visualization. **Xiaojun Yan:** Writing – review & editing, Supervision, Project administration, Resources.

Declaration of Competing Interest

The authors declare that there is no conflict of interest.

Acknowledgments

This study is supported by the Fundamental Research Funds for the Central Universities (Grand No. YWF-21-BJ-J-1140), and National Major Science and Technology Project (J2019-IV-0007-0075, 2017-IV-0012-0049).

Appendix A. The mesh size independence check

First, for the region with refined meshes, different mesh sizes are utilized to conduct the simulation under the condition of **H1-RT**. As shown in Fig. A.1 (a), the $\bar{\varepsilon}$ at microcrack nucleation converges to a fixed value as the mesh is fine enough. Furthermore, as shown in Fig. A.1 (b), the variation of SB width with nominal stress is independent with mesh size, as the element quantity is beyond 5800. Thus, to balance the accuracy and efficiency of computation, the element quantity is determined as 5800 for the region with refined meshes. Secondly, the mesh size independence check for the region with coarse elements is performed. As shown in Fig. A.1 (c), for transition #1 (2932 coarse elements) used in 3.4 Section, we try to refine the elements at the side with coarse meshes, and use transition #2 (3940 coarse elements) to carry out the simulation under the same condition. After refinement, the simulation result basically remains unchanged. To save computation time, it is reasonable to use transition #1 (2932 coarse elements) to conduct the simulation.

Additionally, it worth explaining why the proposed model can pass the mesh size independence check. First, regarding the local model used, previous studies have shown that non-convergence can occur for strain-softening materials, typically in the deformation behavior of the crack tip (Bažant and Jirásek, 2002; de Vuorbeil and Hutchinson, 2020; Shutov and Klyuchantsev, 2021). However, in this study, the SX superalloy is strain hardening, rather than strain softening (Huichen Yu, 2010), and this work does not consider the simulation of crack tip. Moreover, the proposed rate-independent flow rule is distinct from that of non-convergence works. Thus, the mesh size independence of the proposed model can be verified. Secondly, the computations on the evolutions of SB and damage have considered the stress and strain distributions within the element. For instance, the proposed model distributes the damage variable on each element, which is calculated by the stress and strain distributions on each element, rather than some integral or average quantities within the element. Under the framework of FE method, the stress and strain at any points near circular hole will converge to fixed values as the mesh is fine enough. The SB and damage evolutions in proposed model take stress and strain as the inputs and can also pass the mesh size independence check.

Appendix B. The parameter determination method for Ramberg–Osgood formula

To determine the yield stress from stress-strain curve, the Ramberg–Osgood formula is employed to fit the data on curve. The Ramberg–Osgood formula is written as (Ramberg and Osgood, 1943):

$$\bar{\varepsilon} = \frac{\bar{\sigma}}{E'} + \left(\frac{\bar{\sigma}}{K'} \right)^{\frac{1}{n}} \quad (\text{B.1})$$

where E , K' , n' are three unknown parameters. First, for each stress-strain curve, based on the data points at elasticity stage, the E can be determined using linear regression. Then, based on the known E , the Eq. (B.1) is transformed into logarithmic form:

$$\ln\left(\bar{\varepsilon} - \frac{\bar{\sigma}}{E'}\right) = \frac{1}{n'} \ln(\bar{\sigma}) - \frac{1}{n'} \ln(K') \quad (\text{B.2})$$

where $\ln(\bar{\varepsilon} - \frac{\bar{\sigma}}{E'})$ and $\ln(\bar{\sigma})$ follow the linear relationship. So, the parameters K' and n' can be determined using the linear regression. All the calibrated parameters are listed in Table B. 1.

References

- Barnett, M.R., Wang, H., Guo, T., 2019. An Orowan precipitate strengthening equation for mechanical twinning in Mg. *Int. J. Plast.* 112, 108–122.
- Bazant, Z.P., Jirásek, M., 2002. Nonlocal integral formulations of plasticity and damage: survey of progress. *J. Eng. Mech.* 128, 1119–1149.
- Blaber, J., Adair, B., Antoniou, A., 2015. Ncorr: open-source 2D digital image correlation matlab software. *Exp. Mech.* 55, 1105–1122.
- Cervellon, A., Hémery, S., Kürnsteiner, P., Gault, B., Kontis, P., Cormier, J., 2020. Crack initiation mechanisms during very high cycle fatigue of Ni-based single crystal superalloys at high temperature. *Acta Mater.* 188, 131–144.
- Chen, J., Chen, J., Wang, Q., Wu, Y., Li, Q., Xiao, C., Li, S., Wang, Y., Hui, X., 2022. Enhanced creep resistance induced by minor Ti additions to a second generation nickel-based single crystal superalloy. *Acta Mater.* 232, 117938.
- Chen, L., James Edwards, T.E., Di Gioacchino, F., Clegg, W.J., Dunne, F.P.E., Pham, M.-S., 2019. Crystal plasticity analysis of deformation anisotropy of lamellar TiAl alloy: 3D microstructure-based modelling and in-situ micro-compression. *Int. J. Plast.* 119, 344–360.
- Cormier, J., Cailletaud, G., 2010. Constitutive modeling of the creep behavior of single crystal superalloys under non-isothermal conditions inducing phase transformations. *Mater. Sci. Eng.: A* 527, 6300–6312.
- de Vuorbeil, A., Hutchinson, C.R., 2020. A new total-Lagrangian smooth particle hydrodynamics approximation for the simulation of damage and fracture of ductile materials. *Int. J. Numer. Methods Eng.* 121, 2227–2245.
- Dunne, F.P.E., Wilkinson, A.J., Allen, R., 2007. Experimental and computational studies of low cycle fatigue crack nucleation in a polycrystal. *Int. J. Plast.* 23, 273–295.
- Ebrahimzade, V., Haasler, D., Malzbender, J., 2021. Failure mechanism and lifetime of various laser-drilled APS-TBC systems under LCF conditions. *Eng. Fail. Anal.* 127, 105526.
- Fan, Y.S., Tan, L., Yang, X.G., Shi, D.Q., Li, R.Z., Huang, J., Wang, C., 2022. A microstructural rafting state-based constitutive model for single crystal Ni-based superalloys at elevated temperature. *Int. J. Mech. Sci.* 228, 107484.
- Fathallah, K., Chenaoui, A., Darriuelat, M., Dogui, A., 2019. Material rotating frame, rate-independent plasticity with regularization of Schmid law and study of channel-die compression. *Math. Mech. Solids* 24, 18–39.
- Fomin, E.V., Mayer, A.E., Krasnikov, V.S., 2021. Prediction of shear strength of cluster-strengthened aluminum with multi-scale approach describing transition from cutting to bypass of precipitates by dislocations. *Int. J. Plast.* 146, 103095.
- Forest, S., Rubin, M.B., 2016. A rate-independent crystal plasticity model with a smooth elastic–plastic transition and no slip indeterminacy. *Eur. J. Mech. A. Solids* 55, 278–288.

- Forsström, A., Bossuyt, S., Scotti, G., Hänninen, H., 2020. Quantifying the effectiveness of patterning, test conditions, and DIC parameters for characterization of plastic strain localization. *Exp. Mech.* 60, 3–12.
- Guo, X., Zheng, W., Xiao, C., Li, L., Antonov, S., Zheng, Y., Feng, Q., 2019. Evaluation of microstructural degradation in a failed gas turbine blade due to overheating. *Eng. Fail. Anal.* 103, 308–318.
- Guo, Z., Huang, D., Yan, X., 2021a. Physics-based modeling of γ/γ' microstructure evolution and creep constitutive relation for single crystal superalloy. *Int. J. Plast.* 137, 102916.
- Guo, Z., Song, Z., Fan, J., Yan, X., Huang, D., 2021b. Experimental and analytical investigation on service life of film cooling structure for single crystal turbine blade. *Int. J. Fatigue* 150, 106318.
- Guo, Z., Song, Z., Huang, D., Yan, X., 2022. Matrix channel width evolution of single crystal superalloy under creep and thermal mechanical fatigue: experimental and modeling investigations. *Met. Mater. Int.* 28, 2972–2986.
- Gupta, S., Bronkhorst, C.A., 2021. Crystal plasticity model for single crystal Ni-based superalloys: capturing orientation and temperature dependence of flow stress. *Int. J. Plast.* 137, 102896.
- Han, C.-S., Gao, H., Huang, Y., Nix, W.D., 2005. Mechanism-based strain gradient crystal plasticity—I. Theory. *J. Mech. Phys. Solids* 53, 1188–1203.
- Han, Q.-N., Rui, S.-S., Qiu, W., Ma, X., Su, Y., Cui, H., Zhang, H., Shi, H., 2019. Crystal orientation effect on fretting fatigue induced geometrically necessary dislocation distribution in Ni-based single-crystal superalloys. *Acta Mater.* 179, 129–141.
- Huichen Yu, X.W., 2010. Materials Data Manual in Aircraft Engine Design, 4th Edition. Aviation Industy Press, pp. 250–322.
- Kothari, M., 1995. Rate Independent Crystal Plasticity. Department of Mechanical Engineering. Massachusetts Institute of Technology, Cambridge, Boston metro area.
- Larrouy, B., Villechaise, P., Cormier, J., Berteaux, O., 2015. Grain boundary-slip bands interactions: impact on the fatigue crack initiation in a polycrystalline forged Ni-based superalloy. *Acta Mater.* 99, 325–336.
- le Graverend, J.-B., 2019. A hardening-based damage model for fast-evolving microstructures: application to Ni-based single crystal superalloys. *Int. J. Plast.* 123, 1–21.
- le Graverend, J.B., Cormier, J., Gallerneau, F., Villechaise, P., Kruch, S., Mendez, J., 2014. A microstructure-sensitive constitutive modeling of the inelastic behavior of single crystal nickel-based superalloys at very high temperature. *Int. J. Plast.* 59, 55–83.
- Lemaître, J., 1985. A continuous damage mechanics model for ductile fracture. *J. Eng. Mater. Technol.* 107, 83–89.
- León-Cázares, F.D., Schlüter, R., Jackson, T., Galindo-Nava, E.I., Rae, C.M.F., 2020. A multiscale study on the morphology and evolution of slip bands in a nickel-based superalloy during low cycle fatigue. *Acta Mater.* 182, 47–59.
- Leslie, T., Mushongera, P.K., Sangid, M.D., 2020. The interaction of point defects with stress fields generated by persistent slip bands in face-centered cubic nickel. *Adv. Eng. Mater.* 22, 2000490.
- Li, F., Zhang, Y., Wu, Z., Ren, X., Yue, X., Pei, H., Yue, Z., 2022a. Fatigue crack initiation and propagation behavior of nickel-based single crystal DD6 under different drilling processes. *Mater. Sci. Eng.: A* 831, 142246.
- Li, R.Z., Xie, B., Yang, X.G., Fan, Y.S., Sun, Y.T., Shi, D.Q., 2022b. Multi-scale modelling of rafting behaviour under complex stress states for Ni3Al superalloys. *Int. J. Plast.* 152, 103255.
- Li, Z., Gao, H., Wen, Z., Yang, Y., Zhang, Y., Ai, X., Yue, Z., 2020. Microcrack initiation behavior around film cooling holes in a Ni-based single crystal: in situ observation and crystal plastic analysis. *Mater. Sci. Eng.: A* 771, 138609.
- Li, Z., Wen, Z., Gu, S., Pei, H., Gao, H., Mao, Q., 2019. In-situ observation of crack initiation and propagation in Ni-based superalloy with film cooling holes during tensile test. *J. Alloys Compd.* 793, 65–76.
- Ma, A., Dye, D., Reed, R.C., 2008. A model for the creep deformation behaviour of single-crystal superalloy CMSX-4. *Acta Mater.* 56, 1657–1670.
- MathWork <https://www.mathworks.cn/products/matlab.html>.
- Pagan, D.C., Beaudoin, A.J., 2019. Utilizing a novel lattice orientation based stress characterization method to study stress fields of shear bands. *J. Mech. Phys. Solids* 128, 105–116.
- Prastiti, N.G., Xu, Y., Balint, D.S., Dunne, F.P.E., 2020. Discrete dislocation, crystal plasticity and experimental studies of fatigue crack nucleation in single-crystal nickel. *Int. J. Plast.* 126, 102615.
- Ramberg, W., Osgood, W.R., 1943. Description of Stress-Strain Curves By Three parameters, Technical Note No. 902. National Advisory Committee For Aeronautics, Washington DC.
- Reed, R.C., 2008. The superalloys: Fundamentals and Applications. Cambridge University Press.
- Ren, P., Huang, W., Yang, X., Huang, J., Shi, Y., Fan, Y., 2021. A modified constitutive model considering microstructure degradation of Ni-based superalloys and its application to microstructural damage calculation. *J. Alloys Compd.* 882, 160605.
- Sabinis, P.A., Mazière, M., Forest, S., Arakere, N.K., Ebrahimi, F., 2012. Effect of secondary orientation on notch-tip plasticity in superalloy single crystals. *Int. J. Plast.* 28, 102–123.
- Sendrowicz, A., Myhre, A.O., Yasnitskii, I.S., Vinogradov, A., 2022. Stored and dissipated energy of plastic deformation revisited from the viewpoint of dislocation kinetics modelling approach. *Acta Mater.* 237, 118190.
- Shang, Y., Zhang, H., Hou, H., Ru, Y., Pei, Y., Li, S., Gong, S., Xu, H., 2019. High temperature tensile behavior of a thin-walled Ni based single-crystal superalloy with cooling hole: in-situ experiment and finite element calculation. *J. Alloys Compd.* 782, 619–631.
- Shutov, A.V., Klyuchantsev, V.S., 2021. Large strain integral-based nonlocal simulation of ductile damage with application to mode-I fracture. *Int. J. Plast.* 144, 103061.
- Su, Y., Zhang, Q., 2022. Glare: a free and open-source software for generation and assessment of digital speckle pattern. *Opt. Lasers Eng.* 148, 106766.
- Town, J., Straub, D., Black, J., Thole, K.A., Shih, T.I.P., 2018. State-of-the-art cooling technology for a turbine rotor blade. *J. Turbomach.* 140, 071007.
- Vattré, A., Devincret, B., Feyel, F., Gatti, R., Groh, S., Jamond, O., Roos, A., 2014. Modelling crystal plasticity by 3D dislocation dynamics and the finite element method: the discrete-continuous model revisited. *J. Mech. Phys. Solids* 63, 491–505.
- Wang, J., Liang, J., Wen, Z., Yang, Y., Yue, Z., 2019. The inter-hole interference on creep deformation behavior of nickel-based single crystal specimen with film-cooling holes. *Int. J. Mech. Sci.* 163, 105090.
- Wang, Q., Wu, Y., Chen, J., Song, J., Xiao, C., Hui, X., 2022. Enhancement of high temperature low cycle fatigue lifetime of PWA1484 superalloy artificial bicrystals via boron-induced grain boundary strengthening. *Int. J. Fatigue* 165, 107223.
- Wang, Q., Wu, Y., Chen, J., Song, J., Xiao, C., Hui, X., 2023. Insight into the low cycle fatigue deformation mechanisms of minor element doping single crystal superalloys at elevated temperature. *Scr. Mater.* 224, 115151.
- Wang, S., Zhang, Z., 2020. Failure mechanism of turbine guide vane and oxide composition analysis on the surface of failure vane cracks. *Eng. Fail. Anal.* 117, 104763.
- Wen, Z., Li, Z., Zhang, Y., Wen, S., Yue, Z., 2018. Surface slip deformation characteristics for perforated Ni-based single crystal thin plates with square and triangular penetration patterns. *Mater. Sci. Eng.: A* 723, 56–69.
- Westbrooke, E.F., Forero, L.E., Ebrahimi, F., 2005. Slip analysis in a Ni-base superalloy. *Acta Mater.* 53, 2137–2147.
- Xiong Yukai, Z.J., Wei, Rao, Zhiyong, Huang, Guozheng, Kang, Xu, Zhang, 2023. Secondary orientation effects of Ni-based alloys with cooling holes: a strain gradient crystal plasticity FEM study. *Chin. J. Theoret. Appl. Mech.* 55, 120–133.
- Xu, Y., Ruebeling, F., Balint, D., Greiner, C., Dini, D., 2021. On the origin of microstructural discontinuities in sliding contacts: a discrete dislocation plasticity analysis. *Int. J. Plast.* 138, 102942.
- Xu, Y., Xian, J., Stoyanov, S., Bailey, C., Coyle, R.J., Gourlay, C.M., Dunne, F.P.E., 2022. A multi-scale approach to microstructure-sensitive thermal fatigue in solder joints. *Int. J. Plast.* 155, 103308.
- Yang, X.G., Tan, L., Sui, T.X., Shi, D.Q., Fan, Y.S., 2021. Low cycle fatigue behaviour of a single crystal Ni-based superalloy with a central hole: effect of inhomogeneous rafting microstructure. *Int. J. Fatigue* 153, 106467.
- Yin, Q., Wen, Z., Wang, J., Lian, Y., Lu, G., Zhang, C., Yue, Z., 2022. Microstructure characterization and damage coupled constitutive modeling of nickel-based single-crystal alloy with different orientations. *Mater. Sci. Eng.: A* 853, 143761.

- Zhang, C., Hu, W., Wen, Z., Tong, W., Zhang, Y., Yue, Z., He, P., 2019. Creep residual life prediction of a nickel-based single crystal superalloy based on microstructure evolution. *Mater. Sci. Eng.: A* 756, 108–118.
- Zhang, D., He, J., Liang, J., 2020a. Creep rupture mechanism and microstructure evolution around film-cooling holes in nickel-based single crystal superalloy specimen. *Eng. Fract. Mech.* 235, 107187.
- Zhang, J., Zhang, S., Wang, C., Tan, X., 2020b. Recent advances in film cooling enhancement: a review. *Chin. J. Aeronaut.* 33, 1119–1136.
- Zhang, X., Gui, Y., Lai, M., Lu, X., Gu, J., Wang, F., Yang, T., Wang, Z., Song, M., 2023a. Enhanced strength-ductility synergy of medium-entropy alloys via multiple level gradient structures. *Int. J. Plast.* 164, 103592.
- Zhang, X., Zhao, J., Kang, G., Zaiser, M., 2023b. Geometrically necessary dislocations and related kinematic hardening in gradient grained materials: a nonlocal crystal plasticity study. *Int. J. Plast.* 163, 103553.
- Zhang, Y., Xu, Z., Zhu, Y., Zhu, D., 2016. Machining of a film-cooling hole in a single-crystal superalloy by high-speed electrochemical discharge drilling. *Chin. J. Aeronaut.* 29, 560–570.
- Zhang, Z., Wang, W., Jiang, R., Kim, C., Tian, W., Xiong, Y., Zhang, X., Mao, Z., Lee, M.-G., 2022. Tensile behavior of single-crystal superalloy with different structured cooling holes. *Int. J. Mech. Sci.* 229, 107514.
- Zhou, D., Moosbrugger, J.C., Morrison, D.J., 2006. Finite element simulation of PSB macroband nucleation and propagation in single crystal nickel cycled at low plastic strain amplitudes. *Int. J. Plast.* 22, 1336–1366.
- Zhou, H., Zhang, X., Wang, P., Lu, S., 2019. Crystal plasticity analysis of cylindrical holes and their effects on the deformation behavior of Ni-based single-crystal superalloys with different secondary orientations. *Int. J. Plast.* 119, 249–272.
- Zhu, K., Li, C., Pan, B., 2022. Rapid and repeatable fluorescent speckle pattern fabrication using a handheld inkjet printer. *Exp. Mech.* 62, 627–637.